H_2 and CO emission from disks around T Tauri and Herbig Ae pre-main-sequence stars and from debris disks around young stars: warm and cold circumstellar gas [1]

W.F. Thi,[2] E.F. van Dishoeck,[2] G.A. Blake,[3] G.J. van Zadelhoff,[2] J. Horn,[4] E.E. Becklin,[4] V. Mannings,[5] A.I. Sargent,[6] M.E. van den Ancker,[7] A. Natta,[8] J. Kessler[3]

ABSTRACT

[1]Based in part on observations with *ISO*, an ESA project with instruments funded by ESA Member States (especially the PI countries : France, Germany, the Netherlands, and the United Kingdom) and with participation of ISAS and NASA.

[2]Leiden Observatory, P.O. Box 9513, 2300 Leiden, The Netherlands.

[3]Division of Geological & Planetary Sciences, California Institute of Technology 150–21, Pasadena, CA 91125, USA.

[4]Department of Physics and Astronomy, UCLA, Los Angeles, CA 90095–1562, USA.

[5]SIRTF Science Center, MS 314-6, California Institute of Technology, Pasadena, CA 91125, USA

[6]Division of Physics, Mathematics and Astronomy, California Institute of Technology, MS 105-24, Pasadena, CA 91125, USA.

[7]Harvard–Smithsonian Center for Astrophysics, 60 Garden Street, MS 42, Cambridge, MA 02138, USA.

[8]Osservatorio Astrofisico di Arcetri, Largo E. Fermi 5, I–50125 Firenze, Italy.

We present ISO Short-Wavelength-Spectrometer observations of H_2 pure-rotational line emission from the disks around low and intermediate mass pre-main-sequence stars as well as from young stars thought to be surrounded by debris disks. The pre-main-sequence sources have been selected to be isolated from molecular clouds and to have circumstellar disks revealed by millimeter interferometry. We detect 'warm' ($T \approx 100 - 200$ K) H_2 gas around many sources, including tentatively the debris-disk objects. The mass of this warm gas ranges from $\sim 10^{-4}$ $M_\odot$ up to $8{\times}10^{-3}$ $M_\odot$, and can constitute a non-negligible fraction of the total disk mass. Complementary single-dish ^{12}CO 3–2, ^{13}CO 3–2 and ^{12}CO 6–5 observations have been obtained as well. These transitions probe cooler gas at $T \approx 20$–80 K. Most objects show a double-peaked CO emission profile characteristic of a disk in Keplerian rotation, consistent with interferometer data on the lower-J lines. The ratios of the ^{12}CO 3–2/^{13}CO 3–2 integrated fluxes indicate that ^{12}CO 3–2 is optically thick but that ^{13}CO 3–2 is optically thin or at most moderately thick. The ^{13}CO 3–2 lines have been used to estimate the cold gas mass. If a H_2/CO conversion factor of $1{\times}10^4$ is adopted, the derived cold gas masses are factors of 10–200 lower than those deduced from 1.3 millimeter dust emission assuming a gas/dust ratio of 100, in accordance with previous studies. These findings confirm that CO is not a good tracer of the total gas content in disks since it can be photodissociated in the outer layers and frozen onto grains in the cold dense part of disks, but that it is a robust tracer of the disk velocity field. In contrast, H_2 can shield itself from photodissociation even in low-mass 'optically thin' debris disks and can therefore survive longer. The warm gas is typically 1–10 % of the total mass deduced from millimeter continuum emission, but can increase up to 100% or more for the debris-disk objects. Thus, residual molecular gas may persist into the debris-disk phase. No significant evolution in the H_2, CO or dust masses is found for stars with ages in the range of 10^6–10^7 years, although a decrease is found for the older debris-disk star β Pictoris. The large amount of warm gas derived from H_2 raises the question of the heating mechanism(s). Radiation from the central star as well as the general interstellar radiation field heat an extended surface layer of the disk, but existing models fail to explain the amount of warm gas quantitatively. The existence of a gap in the disk can increase the area of material influenced by radiation. Prospects for future observations with ground- and space-borne observations are discussed.

Subject headings: stars: individual (AA Tau, DL Tau, DM Tau, DR Tau, GG Tau, GO Tau, RY Tau, GM Aur, LkCa 15, UX Ori, HD 163296, CQ Tau, MWC 480, MWC 863, HD 36112, AB Aur, WW Vul, V892 Tau, TW Hya, 49 Ceti, HD 135344, Beta Pictoris) — stars: formation — circumstellar matter — molecular processes — infrared: ISM: lines and bands — ISM: molecules

1. Introduction

Recent discoveries of extra-solar giant planets stars have raised questions about their formation (**?**, e.g.)]Butler99,MCM00. Indeed, their characteristics have been a surprise: they orbit much closer to the stars than the planets in our own Solar System and their masses range from that of Saturn up to 10 times the mass of Jupiter ($M_{\rm J} \sim 10^{-3}$ $M_\odot$). These planets are expected to contain a solid core surrounded by a shell of metallic hydrogen and helium and an outer low pressure atmosphere where hydrogen is in the form of H_2 (Guillot 1999; Charbonneau et al. 2000). To build such gaseous giant planets, a large reservoir of H_2 gas is needed at the time of their formation, most likely in the form of a circumstellar disk (**?**, e.g.)]BS96,Bod00.

Most studies of circumstellar material associated with young stars and debris-disk objects rely on con-

tinuum observations of the infrared to millimeter emission produced by heated dust (**?**, e.g.)]BSCG90,SSB97. Dust particles represent only a trace component of disks, however, which have 99% of their mass initially in the form of H_2 gas. Line imaging of trace molecules such as CO with millimeter interferometers reveals the presence of gas in circumstellar disks with sizes of ∼100-400 AU, but the inferred masses are up to two orders of magnitude lower than those deduced from the dust continuum assuming a standard gas/dust ratio and CO/H_2 conversion factor as in molecular clouds (**?**, e.g.)]KS95,MS97,Dut98,MS00,Dent95. The millimeter observations have nevertheless provided compelling evidence for gas in Keplerian rotation around the central star (**?**, e.g.)]SDG00,Dut98. We report here the result of the first spectral survey of the pure-rotational H2 emission lines from circumstellar disks, the only molecule hich can directly constrain the reservoir of warm molecular gas.

A related question is the temperature structure of the circumstellar disks. The radial temperature structure is usually constrained by modeling of the spectral energy distribution assuming either a thin, flat disk geometry (**?**, e.g.)]ALS87 or a flaring disk (**?**, e.g.)]KH87,C91. The dust in these models is heated by radiation from the central star and by the release of energy through accretion. Recent calculations by different groups show substantial differences, however (**?**, e.g.)]Bell97,MHF99,DA98. Specifically, flared disks may have surface layers with temperatures in excess of 100 K out to ∼100 AU (Chiang & Goldreich 1997, 1999). The fitting of spectral energy distributions is known to give ambiguous answers and many disk parameters are still debated because of the non-uniqueness of the fits (**?**, e.g.)]Hen98,BCILNS92. H_2 emission line data can provide direct measurements of the temperature of the warm gas.

According to standard models (**?**, e.g.)]Rud99,Lis93, giant planet formation by core accretion of gas occurs in the first few millions years. Thus, the timescale for the disappearance of the gas compared with that of the dust is of interest. Based on continuum data, Strom et al. (1989), Beckwith et al. (1990), Osterloh & Beckwith (1995) and Haisch, Lada & Lada (2001) suggested that dust disks around T Tauri stars disappear at an age of a few million years. Natta, Grinin & Mannings (2000) searched for evolutionary trends in the outer disk dust mass around Herbig Ae stars. They found no evidence for changes between 10^5 and 10^7 years, but an abrupt transition seems to occur at 10^7 years from massive dust disks to tenuous debris disks. Zuckerman et al. (1995) conducted a survey of CO emission from A-type stars with ages between 10^6–10^7 years and concluded that the gaseous disks disappear within 10^7 years. Determination of the gaseous mass from CO data is hampered, however, by several difficulties compared to that from H_2. Provided that H_2 traces the bulk of molecular gas, it can constrain the time scale for gas dissipation from the disk directly.

Observations of the pure-rotational lines such as the H_2 J=2–0 S(0) 28.218 μm and J=3–1 S(1) 17.035 μm lines are difficult from the ground because of the low terrestrial atmospheric transmission in the mid-infrared. The Short Wavelength Spectrometer (SWS) on board the *Infrared Space Observatory* (ISO) has allowed the first opportunity to observe a sample of T Tauri and Herbig Ae stars, as well as a few young debris-disk objects. The small mass of H_2 implies that the two lowest rotational lines have upper states which lie at rather high energies, 510 K and 1015 K above ground, respectively. The J=2–0 and J=3–1 transitions are thus excellent tracers of the 'warm' ($T \approx$ 80–200 K) component of disks. The mid-infrared H_2 data provide complementary information to ultraviolet H_2 emission (Valenti, Johns-Krull & Linsky 2000) or absorption (Roberge et al. 2001) data toward circumstellar disks, which either probe only a small fraction of the H_2 or depend on the line of sight through the disk and foreground material. H_2 has also been detected at near infrared wavelengths (Weintraub, Kastner & Bary 2001), but since these lines are excited by ultraviolet radiation, X-rays or shocks, they also cannot be used as a tracer of mass.

Spectroscopic observations of H_2 have several advantages over other indirect methods. First, since it is the most abundant gaseous species, no conversion factor is needed. Also, contrary to CO, which has a con-

densation temperature of ∼20 K (Aikawa et al. 1996), it does not freeze effectively onto grain surfaces unless the temperatures fall below ∼2 K (Sandford & Allamandola 1993) — lower than the minimum temperature that a disk reaches. Its photophysics and high abundance allow H_2 to self-shield efficiently against photodissociation by far-ultraviolet photons, such as those produced by A-type stars (Kamp & Bertoldi 2000). Moreover, because the molecule is homonuclear, its rotational transitions are electric quadrupole in nature, and thus possess small Einstein A-coefficients. On the one hand, this presents an observational problem since high spectral resolution is required to see the weak line on top of the usually strong mid-infrared continuum. On the other hand, the benefit is that the lines remain optically thin to very high column densities, making the radiative transfer simple. Another disadvantage is that the lines are only sensitive to warm gas and cannot probe the bulk of the (usually) cold circumstellar material probed by CO $J = 1 - 0$ and $J = 2 - 1$ interferometric observations. Also, the high continuum optical depths at 28 μm prevent observations into the inner warm mid-plane of the disk. As a complement, the same stellar sample has therefore been observed in the ^{12}CO and ^{13}CO $J = 3 - 2$ lines with the *James Clerk Maxwell Telescope* and the ^{12}CO $J = 6 - 5$ line with the *Caltech Submillimeter Observatory*. These transitions probe lower temperatures than H_2, about 20–80 K in the regime where the dust is optically thin. The combination of H_2 and CO observations is sensitive to the full temperature range encountered in disks. Along with millimeter continuum observations taken from the literature, such data can provide a global picture of the structure and evolution of both the gas and dust components of circumstellar disks.

The paper is organized as followed. We first justify the choice of the objects in our sample (§2). In §3, a description of the observations is provided with emphasis on the special data reduction method used for the H_2 lines. In §4 and 5, the data are presented and physical parameters such as mass and temperature are derived from our observations of H_2 and CO lines, as well as from 1.3 millimeter continuum fluxes taken from the literature. The accuracy of each method is assessed. In §6, the different results are compared and possible trends with effective temperature of the star or age are investigated and the possible origin of the warm gas is mentioned briefly. Finally, a discussion of the gas content in debris-disk objects is given. The results for one object, the double binary GG Tau, have been presented by Thi et al. (1999a). Earlier accounts of this work may be found in van Dishoeck et al. (1998) and Thi et al. (1999b), whereas the debris-disk sources are discussed in Thi et al. (2001). Stapelfeldt, Padgett & Brooke (1999) present searches for H_2 emission in a complementary set of weak-line T Tauri objects.

2. Objects

Our study focuses on two classes of pre-main-sequence stars with transitional ages spanning 10^6–10^7 years. T Tauri stars in the sample have spectral types of Me and Ke, corresponding to stellar masses in the range from 0.25 to 2 $M_\odot$ and are probably younger analogs to the Sun. The higher-mass Herbig Ae stars (2–3 $M_\odot$) share the spectral type of debris-disk sources and may be considered as younger counterparts to the debris-disk objects. In addition, three young debris-disk objects, namely 49 Ceti, HD 135344 and β Pictoris are included in our sample. The choice of objects is based on several criteria in order to maximize the chance to detect the faint H_2 lines on top of the mid-infrared continuum and to avoid confusion with emission from remnant molecular cloud material. First, the observed stars exhibit the strongest 1.3 millimeter fluxes in the survey of T Tauri stars by Beckwith et al. (1990) and Herbig Ae stars by Mannings & Sargent (1997, 2000), i.e., they possess the highest dust disk masses among the T Tauri and Herbig Ae stars in the Taurus-Auriga cloud. Second, they have all been imaged with millimeter interferometers in CO and dust continuum and show evidence for Keplerian disks. The only exceptions are UX Ori and WW Vul, where no CO is detected.

Third, the sample is biased toward sources with a weak mid-infrared continuum at 10–30 μm to improve the line-to-continuum contrast. This also prevents instrumental fringing problems. A faint mid-infrared excess suggests that a 'dust hole' exists in the disk close to the star, which may be caused by settling and coagulation of dust particles in the mid-plane (Miyake & Nakagawa 1995), to clearing of the inner part of the disk by small stellar companion(s) or proto-planet(s) (**?**, e.g.)]Lin00 or to shadowing of part of the disk (Natta et al. 2001). Finally, most of these stars are located in parts of the Taurus cloud where the CO emission is very faint or absent. Our original sample also included objects in Ophiuchus (van Dishoeck et al. 1998), but these have been discarded from this sample because of confusion by cloud material.

HD 135344, 49 Ceti and β Pictoris have been identified as debris-disk objects based on their far-infrared excess above the expected photospheric flux level (e.g. Backman & Paresce 1993). Keck 20 μm images reveal the presence of dust disks around the first two sources (Koerner 2000, Silverstone et al., private communication) whereas β Pictoris has been imaged at many wavelengths (**?**, e.g.)]LBA01. HD 135344, however, shows strong single-peaked Hα emission (Dunkin, Barlow, & Ryan 1997), suggesting that it also has Herbig Ae-type characteristics. The three debris-disk sources are objects located far from any molecular cloud.

This work does not constitute a statistical study since the sample is limited in number and biased toward the highest disk masses and low mid-infrared continuum. In Table 1 the stellar properties of objects of our sample are tabulated, including coordinates, effective temperature, luminosity, and distance, together with references to relevant literature.

3. Observations

3.1. ISO-SWS observations

The H_2 $J = 2 - 0$ S(0) line at 28.218 μm and the $J = 3 - 1$ S(1) line at 17.035 μm were observed with the ISO-SWS grating mode AOT02 (de Graauw et al. 1996). Typical integration times were 600–1000 s per line, in which the 12 detectors were scanned several times over the 28.05–28.40 and 16.96–17.11 μm ranges around the lines. The H_2 $J = 5 - 3$ S(3) 9.66 μm and $J = 7 - 5$ S(5) 6.91 μm lines were measured in parallel with the S(0) and S(1) lines, respectively, at virtually no extra time. The spectral resolving power $\lambda/\Delta\lambda$ for point sources is $\sim$2000 at 28 μm and $\sim$2400 at 17 μm. The SWS aperture is $20'' \times 27''$ at S(0), $14'' \times 27''$ at S(1), and $14'' \times 20''$ at S(3) and S(5). For a few sources, observations of the S(1) line at a $1'$ off position have been obtained as well. The S(2) J=4–2 12 μm line was also searched for toward 49 Ceti and HD 135344.

The continuum provides narrow band photometry. Since the observing procedure does not perform spatial chopping, no zodiacal or background emission is subtracted. The zodiacal background component has a continuous spectrum corresponding to a dust temperature of about 260 K (Reach et al. 1996) with an estimated flux density in the SWS aperture of about 0.3 Jy, so that it can contaminate the continuum emission in some of our faintest objects. Continuum fluxes above 3 Jy are considered as coming essentially from the sources (star+disk) alone.

3.1.1. Data reduction

The expected peak flux levels of the H_2 lines are close to the sensitivity limit of the instrument. In order to extract the H_2 lines, special software designed to handle weak signals on a weak continuum was used for the

data reduction in combination with the standard Interactive Analysis Package. The details and justification of the methods used in the software are described elsewhere (Valentijn & Thi 2000) and summarized below (see also the ISO-SWS manual at http://www.iso.vilspa.esa.es/users/expl_lib/SWS_top.html).

The raw data consist of 12 non-destructive measurements per elementary integration (reset) corresponding to the 12 single-pixel detectors, hence 24 observed points for a 2 second reset. A single scan lasts 200 seconds and typically 3–5 scans per line have been obtained, corresponding to 7200–12000 data points. Since the readout system acts as a capacitor, the signal has the form of an exponential decay, and this curvature is first corrected using the AC time constant obtained during the pre-flight calibration phase. Then a correction of the instantaneous response function, or 'pulse-shape', is applied with the level of the correction determined from the data themselves because the shape varies in time, a procedure called 'self-calibration'. Finally, a cross-talk correction is performed. This chain of calibration results in removing the curvature and improving the straightness of the observed slope which is in fact the measure of the flux. It also increases appreciably the photometric accuracy and allows a better subsequent determination of the noise.

Other factors, such as dark current drifts, influence the sensitivity limit of the instrument as well and have to be corrected. The majority of noisy data points are actually caused by impacts of cosmic rays, called glitches, either on the detectors or on the readout electronics. The level of cosmic ray hits fluctuates markedly, depending on the position of the satellite and the activity of the Sun. The rate of glitches may vary from scan to scan. At the level we are interested in, up to 50% of the data points can be rendered unusable by cosmic rays or other instrumental artifacts.

Cosmic rays not only affect the sensitivity of the detectors instantaneously, but also for some longer recovery time, a phenomenon called the post-glitch effect. Most of the time, the glitches are secondary electron-hole pairs created by the interaction of the energetic particles with the detector elements; while the lifetime of these pairs is short, other consequences of the impact can last longer. The decay of this effect is observed to have an exponential form. The observing procedure used by the SWS allows investigators to track events emerging simultaneously in more than one detector. These so-called 'correlated-noise events' appear as a spurious feature in emission or sometimes in absorption with a gaussian profile whose width is close to the resolution of the instrument. The gaussian-like profile comes from the fact that the glitch affects several detectors simultaneously, which results in a shift in wavelength in the final spectrum.

In order to detect and circumvent the glitches, four types of statistical filters have been defined. The first two are standard filters also employed in the SWS pipeline software; the last two are additions by us. The software is written in *IDL* (Interactive Data Language). Each of these filters generates an array of non-valid points detected by the adopted statistical method characterized by a unique parameter. Thus, careful choices of filter parameters are crucial in determining the quality of the resulting spectrum. The arrays are then cross-correlated. Most of the time, the glitches are detected by more than one filter and those points are immediately discarded.

The first filter consists in removing points which have a flux outside a specified range defined by the user. This procedure may seem artificial, but is justified by the fact that both line and continuum fluxes are faint. In our data, this method removes points 5 sigma above the continuum standard deviation calculated using all points. The second filter searches for data points with a standard deviation of the slope-fitting higher than the standard value adopted in the SWS pipeline. This filter is efficient when used after the self-calibration procedure described above. The third filter has been set up specifically in this work to detect correlated noise. This filter detects the glitches which are discrete stochastic events in the time domain. The data from the 12 detectors observed at a single time are summed, and the mean and standard deviations are

computed. If the standard deviation is higher than a specified parameter ϕ, the data points are considered as glitches and are discarded in all 12 detectors. The value of ϕ, which is a multiple of the standard deviation σ, $\phi = n \times \sigma$, is difficult to determine *a priori* and can vary from scan to scan. Indeed, the computed σ is affected by the number of cosmic ray hits — a high rate of glitches results in a high standard deviation— so that ϕ has to be small. We have therefore used an automated procedure to find the optimum values of ϕ_i, in which each spectrum is examined with a range of values of ϕ_i from n=1–6 times the standard deviation for each individual scan i with a step of 0.5. Thus, for a typical case of 3 scans, 10^3 versions of the reduced spectrum are generated. The fourth step removes additional points one or two resets after a glitch is detected by the previous technique.

The data reduction procedure results in a "dot cloud" of observed fluxes as functions of wavelength. As a final step, convolution with a gaussian whose FWHM is set by the theoretical resolution of ISO-SWS at the relevant wavelength is done. We have chosen to use a flux-conserving interpolation which can modify the resolution but does not change the total integrated flux. Since the lines are not spectrally resolved, the line profile is not relevant. Small velocity shifts of the line of order 30 km s^{-1} compared with the rest wavelengths are frequent. Many parameters can cause such a shift, including the low signal-to-noise of the data or pointing offsets. The latter problem not only affects the peak position but also the flux since the beam profile is highly dependent on the position in the entrance slit of the spectrometer. Because the H_2 emission can arise from a region 1–2″ offset compared to the position of the star, additional shifts of the order of a few tens of km s^{-1} are possible. The 1000 spectra are then sorted by number of remaining data points. Generally, the noise level due to glitches tends to decrease significantly as the number of points decreases until a minimum is reached when the statistical noise takes over because of the small number of data points left. With this non-standard data reduction procedure, it is difficult to devise an objective detection criterion. Therefore, we adopt the following definition of the level of confidence in our detections, depending on the final S/N of the spectrum as well as the fraction of reduced spectra in which the line is clearly seen. A line is considered to be detected when the S/N is 3 or higher and if its profile lies within a gaussian mimicking the line profile of an extended source filling the entire beam . Observations which are only slightly affected by cosmic ray hits show detections in a large number of the reduced spectra ($>$ 75% of the 1000 spectra). The level of confidence of the detection is considered "high" in those cases. The level becomes "medium" when the detection is present in about 50–75% of the spectra. In cases of non-detection, the line is seen in less than 50% of the reductions. Ultimately, we cannot rule out possible instrumental artifacts which are not detected by our filters.

Of all the possible reductions, the spectrum with the lowest continuum fluctuation (fringing) and noise and the highest S/N of the line is kept as our best reduced spectrum and plotted in this paper. The criterion of high peak flux and S/N comes from the fact that the filters described above eliminate not only noisy data points but also some valid points to a certain level. To keep this level as low as possible, a compromise between quality (i.e., S/N) and flux level is adopted.

The non-gaussian nature of the noise makes the overall error difficult to estimate, and we assume a fiducial 30% photometric uncertainty in the rest of the paper. This error is propagated into all the resulting temperatures and masses. The actual uncertainty may be larger due to the low S/N of the data, but cannot be quantified in a consistent way for different sources. Note that the above procedure only throws away data points and therefore cannot create artificial lines. This is confirmed by the absence of lines at blank sky, or off-source, positions reduced with the same procedure.

The above method was adopted for all sources with a weak continuum level ($<$3 Jy). For sources with a strong mid-infrared continuum (AB Aur, HD 163296, RY Tau, CQ Tau, MWC 863), the fringing effect on the

continuum becomes the limiting factor for detection. Errors in the dark current subtraction are a possible cause of this fringing. For these sources, the fringes have been minimized by varying the dark current level.

3.2. CO observations

As a complement to the ISO-SWS data, we have observed the same sample of T Tauri and Herbig Ae stars in various moderate- to high-J CO transitions between 1998 and 2000 with submillimeter single-dish telescopes. Previous studies have observed the lowest J=1–0 and/or $2-1$ transitions, either with interferometers (Koerner & Sargent 1995; Dutrey et al. 1996; Mannings & Sargent 1997, 2000) or with single dishes (**?**, e.g.)]Dut97, but no homogeneous data set using the same line, isotope and telescope exists for our sources. We focus here on the higher-J 3–2 and 6–5 transitions to probe gas with T=20–80 K.

Observations of the ^{12}CO and ^{13}CO $J = 3-2$ lines were carried out at the *James Clerk Maxwell Telescope* (JCMT)[9] using the dual polarization receiver B3 as the frontend and the Digital Autocorrelator Spectrometer (DAS) as the backend. Data were acquired with a beam switch of $180''$ and, in cases of extended emission, also a position switch up to $30'$. To check for extended emission, several positions offset by $30''-60''$ were observed as well. Since the FWHM beam size of the JCMT at 345 GHz is $14''$ and the extent of the disks at the distance of Taurus is at most $5''$, the observations suffer from large beam dilution, as do the H_2 data. The receiver was tuned single sideband, with typical system temperatures above the atmosphere ranging from 400–600 K. The spectral resolution was typically 0.13 km s^{-1}, sufficient to resolve the line profiles, but the data are Hanning-smoothed once to improve the signal-to-noise. The final spectral resolution is 0.26 km s^{-1}. Integration times were typically 10–20 minutes for ^{12}CO and up to 2 hrs for ^{13}CO reaching a typical rms noise of $\sim$ 15 mK. The antenna temperatures have been converted to main beam temperatures using a main beam efficiency at 330 GHz of $\eta_{\rm MB}$=0.62 obtained from observations of planets by the JCMT staff (see http://www.jach.hawaii.edu/JACpublic/JCMT/rx/b3/cal.html). The data reduction was performed using the SPECX and CLASS software.

The ^{12}CO $J = 6-5$ data were obtained with the *Caltech Submillimeter Observatory* (CSO)[10] using the sensitive 650 GHz receiver of Kooi et al. (1998) in double-sideband mode. Two acousto-optical spectrometers with resolutions of 0.05 and 0.5 km s^{-1} were used as the backends. Typical system temperatures under excellent weather conditions were $\sim$ 2000 K. The CSO beam size at 650 GHz is $\sim 14.5''$, comparable to the JCMT beam at 330 GHz, and the main beam efficiency is $\eta_{\rm MB}$=0.40.

4. H_2 results and derived parameters

4.1. ISO-SWS spectra

The final continuum subtracted H_2 spectra are presented in Figures 1 and 2 for the J=2–0 S(0) and 3–1 S(1) lines respectively. The typical rms noise level is 0.2–0.3 Jy. The dash-dotted lines in Figure 1 and

[9]The James Clerk Maxwell Telescope is operated by the Joint Astronomy Centre on behalf of the United Kingdom Particle Physics and Astronomy Research Council, the Netherlands Organisation for Scientific Research, and the National Research Council of Canada

[10]The Caltech Submillimeter Observatory is operated by the California Institute of Technology under funding from the US National Science Foundation, contract AST–9980846

2 indicate the wavelength range in which the H_2 line is expected, taking into account the possible velocity shifts discussed in §3. As explained in §3, our line profiles may differ from the nominal instrumental profile in width because of the adopted interpolation scheme. The H_2 line positions and basic molecular data are listed in Table 2, whereas the H_2 S(0) and S(1) integrated fluxes are reported in Table 3. The S(3) and S(5) lines are not detected in any of the objects with an upper limit of $\sim 4\times10^{-15}$ erg s^{-1} cm^{-2} (3σ). The level of confidence of a detection is indicated in the right-hand column of Table 3. Similarly, the S(2) line is not detected toward 49 Ceti or HD 135344 with an upper limit of $\sim 9\times10^{-15}$ erg s^{-1} cm^{-2}. Both the S(2) and S(3) lines are located in a wavelength region where silicate features in emission or absorption are strong.

Lines are detected in several disks around T Tauri and Herbig Ae stars, with no apparent trend with age or spectral type (see §6.2). There are also likely detections of lines toward the debris-disk objects, especially from HD 135344 and β Pictoris.

The S(1) line shows a wider spread in observed fluxes and is more readily detected for several reasons. First, the Einstein-A coefficient for the $J=3-1$ line is a factor of 16.5 larger than that of the $2-0$ line. Also, the spectral resolution is somewhat higher at 17 μm than at 28 μm and the continuum lower, so that the line-to-continuum ratio is larger. Finally, the sensitivity of the 17 μm detectors is better. All of these factors explain why the S(1) line is more easily seen than the S(0) line, in spite of the fact that the $J=3$ level has a factor of 40 lower population than the $J=2$ level in gas with an estimated temperature of around 100 K.

4.2. Contamination by diffuse H_2 emission?

Except for the case of β Pictoris, the ISO-SWS beam is much larger than the typical sizes of the circumstellar disks of $<5''$. Thus, care has to be taken that the H_2 emission is not affected by any remnant cloud or envelope material in the beam. Observations of the S(1) line have been obtained at several off source positions $1'$ south. Toward 49 Ceti and HD 135344, which are far away from any molecular cloud, no emission is detected off source at the level of 8×10^{-15} erg s^{-1} cm^{-2} rms, consistent with the expectation that diffuse atomic gas does not emit in H_2 lines. A weak S(1) line of $\sim 10^{-14}$ erg s^{-1} cm^{-2} is seen $1'$ south of LkCa 15. This flux probably comes from a background cloud at a different velocity than that of the source (see below).

Strong H_2 lines have been detected with the SWS toward embedded Herbig Ae and T Tauri stars where ultraviolet photons and shocks interact with the surrounding material, but in these cases the observed excitation temperatures of 500–700 K are much higher than those found for our objects van den Ancker, Tielens, & Wesselius (2000a); van den Ancker et al. (2000b). Searches for H_2 lines toward diffuse molecular clouds with $A_V = 1-2$ mag have been performed by (Thi et al. 1999c), but no lines are detected at the level of 8×10^{-15} erg s^{-1} cm^{-2} rms for clouds with densities less than 10^3 cm^{-3} and incident radiation fields less than 30 times the standard interstellar radiation field. The strengths of the S(0) and S(1) lines from diffuse clouds can also be estimated from ultraviolet observations of H_2 obtained with the *Copernicus* satellite and the *Far-Ultraviolet Space Explorer* (FUSE) (Spitzer & Jenkins 1975; Shull et al. 2000). Consider as an example the recent FUSE results for the translucent cloud toward HD 73882 (A_V=2.4 mag) by Snow et al. (2000). The observed column densities in J=2, 3 and 5 translate into fluxes of 2.7×10^{-14}, 1.2×10^{-13} and 1.1×10^{-13} erg s^{-1} cm^{-2} for the S(0), S(1) and S(3) lines, respectively, assuming the gas fills the ISO-SWS beam. The S(0) and S(1) fluxes are comparable to our observed values, but the S(3) flux is significantly higher than our upper limits. Indeed, both the *Copernicus* and FUSE data give typical excitation temperatures for the

J=2–7 levels of ∼300 K, significantly larger than the values of ∼100–200 K found here. Moreover, such thick clouds as those toward HD 73882 or ζ Oph emit significant CO emission (**?**, e.g.)]GvDB94,vD91, which is generally not observed at the off source positions in our sample.

To check for the presence of molecular gas at off-source positions, mini-maps in ^{12}CO 3-2 have been obtained in steps of 30″ for most of our sources (see also §5). For GG Tau, LkCa 15, MWC 480 and GM Aur, no emission is found off source down to 30 mK rms at the velocity of the sources. In other cases such as GO Tau, DR Tau, HD 163296, weak off-source emission is seen in ^{12}CO 3–2 with velocities shifted compared to the source velocity, but this off-source emission is not seen in ^{13}CO 3–2. The off-source CO emission is at least a factor of 30 lower than found for translucent clouds such as HD 73882. Thus, the bulk of the molecular gas for these sources is clearly located in the disks, but some lower-density cloud material may be present. Based on the above arguments combined with the absence of S(3) emission, this diffuse gas is expected to make only a small contribution to the S(0) and S(1) lines. Finally, two of our objects, AB Aur and RY Tau, show single dish CO data which are clearly dominated by more extended remnant envelope material. In these cases, a significant fraction of the H_2 emission may arise from extended gas although the temperature in the envelope (10–20 K) may be too low to produce substantial rotational excitation.

In summary, for most of our sources, the H_2 emission is unlikely to be contaminated by extended emission from diffuse molecular gas, but this cannot be ruled out for cases such as AB Aur. In fact, H_2 ultraviolet absorption toward AB Aur has been detected by FUSE (Roberge et al. 2001) and arises in an extended low-density envelope around the star or from general foreground material.

4.3. H_2 temperatures

The integrated flux F_{ul} of a rotational emission line $J_u \rightarrow J_l$ of H_2, assuming that the line is optically thin and not affected by dust extinction, and that the gas is at a single temperature $T_{\rm ex}$, is given by

$$F_{ul} = \frac{hc}{4\pi\lambda} N(\mathrm{H_2}) A_{ul} x_u \Omega \ \mathrm{erg\ s^{-1}\ cm^{-2}}, \quad (1)$$

where λ is the wavelength of the transition, A_{ul} is the spontaneous transition probability, $N(H_2)$ the total column density of H_2 and x_u the population of level u. Ω corresponds to the source size, which is not known since the H_2 data are spatially unresolved. For gas densities larger than 10^3 cm^{-3}, the lines are thermalized and the population x_u follows the Boltzmann law

$$x_u = (2J_u + 1) g_N \exp\left(-E_{J_u}/kT_{\rm ex}\right)/Q_{\mathrm{H_2}}(T_{\rm ex}), \quad (2)$$

with E_{J_u} being the energy of the upper level, $Q_{\mathrm{H_2}}(T_{\rm ex})$ the partition function of H_2 at $T_{\rm ex}$ and g_N the nuclear statistical weight factor, which is 1 for para-H_2 (even J) and 3 for ortho-H_2 (odd J). The lines are optically thin up to column densities of 10^{23} cm^{-2} owing to the low values of the Einstein $A-$coefficients.

When both the S(0) and S(1) lines are detected, the excitation temperature can be obtained from the relation

$$T_{\rm ex} = \frac{505.24}{\ln\left(112.51 \times F_{20}/F_{31}\right)} \ \mathrm{K}. \quad (3)$$

In LTE, $T_{\rm ex}$ is equal to the kinetic temperature T. F_{20} and F_{31} are the integrated S(0) $J = 2 - 0$ and S(1) $J = 3 - 1$ fluxes, respectively. Since no data are available to constrain the ortho-H_2 to para-H_2 ratio, we assume that the ortho/para ratio is in LTE at the temperature $T = T_{\rm ex}$. At T=100 K, the ortho/para ratio is 1.6. No correction for differential extinction between the S(0) and S(1) lines is applied.

The inferred temperatures range from 100 to 200 K (see Table 3). The uncertainty of 30% in the fluxes propagates into a ∼10% error in the temperature. If the emission were affected by ∼30 magnitudes of extinction, the derived temperatures would be increased by typically ∼20 K, illustrating that this does not have a large effect. The upper limits on the S(3) line translate into upper limits on the gas temperature of typically < 250 K if no correction for differential extinction is made. Similarly, the upper limits on the S(2) line imply temperatures <200 K for HD 135344 and 49 Ceti. The detection of either the S(0) or S(1) lines combined with the upper limits on S(3) imply a probable temperature range of 100–200 K for the gas.

4.4. Warm gas masses from H_2

Because the lines are optically thin, the measured fluxes can be translated directly into a beam-averaged column density of warm gas using Eq. (1) with Ω equal to the solid angle of the ISO-SWS beam at the observed wavelength. The gas mass can be computed from

$$M_{\rm warm\ gas} = 1.76\ 10^{-20}\ \frac{F_{ul}\ d^2}{(hc/4\pi\lambda)\ A_{ul} x_u}\ {\rm M}_\odot \qquad (4)$$

where in addition to the above assumptions, d is the distance in pc which is provided by the Hipparcos satellite or taken from the literature (see Table 1). The derived masses are presented in Table 3 and depend strongly on the population x_u and thus on the temperature T. This is illustrated in Figure 3, which shows the inferred mass as a function of temperature for a S(1) line flux of 10^{-13} erg s^{-1} cm^{-2} at the distance of Taurus (140 pc): for temperatures between 100 and 200 K, the mass changes by approximately one order of magnitude. Assuming an error on the flux of ∼30% and including an error on the distance of 10%, the error on the mass reaches ∼55% in cases where both the S(0) and S(1) lines have been measured. When only one line is detected, a range of masses is obtained by assuming that the excitation temperature lies between 100 and 200 K and consequently shows a large spread.

If the line emission were affected by 30 magnitudes of extinction, the derived masses are changed by less than 20%: the increase in mass due to the extinction correction is compensated by its decrease owing to the higher inferred temperature (see §4.3).

4.5. Mid-infrared continuum: tracing the warm dust

The continuum around the lines can be used to perform narrow band photometry and the resulting absolute fluxes are given in Table 4. Moreover, data in the 3.4 μm region have been obtained in parallel and are included. The values at 28 μm are consistent, within the errors (estimated to be ∼ 30%), with the IRAS Point Source Catalog fluxes extrapolated from observations at 25 μm. As mentioned in §3, the sources with faint mid-infrared continuum fluxes (< 1 Jy) can be contaminated by zodiacal emission and include a contribution from the star. Typically, for a star located in the Taurus cloud with an effective temperature $T_{\rm eff}$=8700 K and luminosity $\log(L/L_\odot)$=1.5, the stellar monochromatic fluxes are 0.26, 0.04, 0.16, 3 10^{-3} and 7 10^{-4} Jy at 3.4, 6.9, 9.6, 17 and 28 μm respectively. Thus, the stellar contributions at 17 and 28 μm are negligible compared to the zodiacal emission.

A complete understanding of the mid-infrared line and continuum emission requires a detailed radiative transfer code and a specific disk model implying many assumptions. We adopt here a simplified picture based on the Chiang & Goldreich (1997) model of irradiated passive disks. The disk is divided into 3 components:

(i) a hot part giving rise to the near-infrared emission; (ii) a warm part ($T_{\rm dust}$ ≈80–300 K) responsible for the mid-infrared emission, and perhaps also the H_2 emission; and (iii) a cold part ($T_{\rm dust}$ <80 K) giving the submillimeter continuum and the CO emission. Component (ii) corresponds to the warm surface layer in the Chiang & Goldreich models. Component (i) is not present in those models, but may be due to very hot thermal emission in an inner boundary layer, or to non-thermal emission by very small grains or PAHs (van den Ancker et al. 2000b; Sylvester, Skinner & Barlow 1997), from Fe-containing grains (Bouwman et al. 2000) or to due a very hot inner layer (Natta et al. 2001). Our main reason for this partition is to compare separately the 'warm' and 'cold' gas and dust components.

To obtain a rough estimate of the temperature of the warm dust, the 17/28 μm flux ratios have been fitted with an optically thin dust model, as may be appropriate for the surface layers of disks. The grain emissivities of Ossenkopf & Henning (1994) have been used. Figure 4 shows the resulting warm dust temperature for different values of the 17/28 μm ratio. The observed values are included in Figure 4 and the resulting fits are summarized in Table 4. The observational errors on the temperature are ∼10%. Interestingly, the beam average warm gas temperatures derived from H_2 are higher by 20–50 K (see Figure 5). There are several possible explanations of this difference, e.g. the location of the emitting gas and dust may be different or a gas heating mechanism other than gas-grain collisions has to be invoked.

5. CO results and derived parameters

5.1. ^{12}CO and ^{13}CO 3–2 lines

Observations of ^{12}CO 3–2 lines have been performed with the JCMT toward most of the sources observed with ISO, plus a few other T Tauri and Herbig Ae stars. In all but a few cases, the ^{12}CO 3–2 and ^{13}CO 3–2 lines are detected with good signal-to-noise ($> 5\ \sigma$), and the spectra are presented in Figures 6 and 7. The lines show the typical double-peaked profile consistent with emission from a disk in Keplerian rotation seen at a certain angle (**?**, e.g.)]BS93,Gui99. The full width at half maximum of the line profile is typically 2.5–3 km s^{-1} and the separation between the two peaks is of order of 1.2–2 km s^{-1}. The integrated fluxes are computed by fitting two gaussians, which are tabulated in Table 5. The uncertainty in the integrated fluxes is dominated by the calibration error of ∼30 %. The mean integrated area of the ^{12}CO 3–2 line for the T Tauri stars is ∼0.5 K km s^{-1} higher than that for Herbig Ae stars. The clear presence of the double peak suggests that the microturbulence in these disks is no more than 0.2-0.3 km s^{-1}, comparable to the thermal width of ∼0.22 km s^{-1} at 30 K. CO 3–2 is not detected toward CQ Tau. This non-detection is compatible with the CO 2–1 flux detected by Mannings & Sargent (2000) using the Owens Valley Millimeter Array.

A clear ^{12}CO 3–2 disk line profile is also detected toward the debris-disk object HD 135344, previously studied in ^{12}CO 2–1 by Coulson & Walther (1995). No 3–2 searches have been performed toward 49 Ceti, but Zuckerman et al. (1995) report a detection of the CO 2–1 line. A deep search for ^{12}CO 2–1 has been performed toward β Pictoris by Liseau & Artymowicz (1998) with a limit of 11 mK rms in the 23″ SEST beam. CO is seen by ultraviolet absorption lines, however, and Roberge et al. (2000) infer a column density of (6.3 ±0.3) 10^{14} cm^{-2} of CO gas at a temperature of 20–50 K.

Figure 9 shows the ^{13}CO 3–2 versus ^{12}CO 3–2 integrated line fluxes normalized to a distance of 100 pc. The different regimes of optical depth are indicated. The data fall in the region where ^{13}CO 3–2 is thin whereas ^{12}CO 3–2 is optically thick. No difference is found between the T Tauri and the Herbig Ae stars. Assuming a [^{12}C]/[^{13}C] ratio of 60 and the same excitation temperature for ^{12}CO and ^{13}CO, the beam-averaged optical depths $\bar{\tau}$ of the ^{13}CO 3–2 line can be calculated, and are given in the last column of

Table 5. If the excitation temperature of ^{12}CO is higher than that of ^{13}CO, as suggested by models of van Zadelhoff et al. (2001), $\bar{\tau}$ could be increased by a factor of two. Nevertheless, a low optical depth $\bar{\tau} < 1$ of ^{13}CO 3–2 is confirmed by the non-detection of C^{18}O 3–2 emission (van Zadelhoff et al. 2001). Thus, the ^{13}CO 3–2 line could constitute a tracer of the total gas mass in the outer part of disks provided the excitation temperature can be determined and the ^{13}CO/H_2 conversion factor is known.

As mentioned in §4.4, ^{12}CO 3–2 observations have also been obtained at positions offset from the sources, in particular for a 30″ offset (two JCMT beams). In all cases, the double-peaked line profile disappears completely at the off position, confirming that it arises from the circumstellar disk. In some sources, however, a narrow profile at a velocity slightly offset from that of the disk remains. This emission is due either to remnant envelope material or the general molecular cloud from which the star formed. Its strength is uncertain up to a factor of two since it was not possible to find a good off-position in all cases. For the specific case of LkCa 15, no emission was found at 30″ offset, but a weak ^{12}CO 3–2 line with $T_{\rm MB}$=0.22 K appeared at $V_{\rm LSR} = -8$ km s^{-1} at the 1′ south position, where the H_2 S(1) off-source spectrum was taken. This CO emission is more than 10 km s^{-1} offset from the velocity of the star and is most likely the result of a chance coincidence with a background cloud.

5.2. ^{12}CO 6–5 lines

^{12}CO 6–5 emission is detected toward several sources using the CSO (see Figure 8). Weak, but clear double-peaked profiles are seen from disks such as those around LkCa 15 and MWC 480 (**?**, see also)]GJ01. The line is particularly strong toward AB Aur, likely because of the extended envelope. Indeed, a small ^{12}CO 3–2 and 6–5 map around the source shows strong lines even at one beam offset. The integrated fluxes are reported in Table 6.

The 6–5 line probes preferentially gas at higher temperatures around 100 K, but its high optical depth decreases the excitation conditions to lower temperatures. The ratio of the 6–5/3–2 line intensity is a measure of this temperature (van Zadelhoff et al. 2001). A full analysis requires a 2-D radiative transfer calculation for disk models with different radial and vertical temperature profiles. However, a rough estimate can be obtained from a simple 1-D escape probability formalism assuming an iso-thermal and iso-density slab in which the abundances are chosen such that the ^{12}CO 6–5 and 3–2 lines are optically thick. This slab would be representative of the intermediate and surface layers of disks, from which most of the emission is thought to arise.

This simple analysis shows that the sources have a range of temperatures. The upper limit on the CO 6–5 line for RY Tau indicates a cool emitting region of about 10 K. The sources LkCa 15, AB Aur, GG Tau and GM Aur all have relatively low temperatures between 20 and 50 K, but these ranges can be extended considerably if typical calibration errors of 20% are taken into account, especially for GG Tau and AB Aur. The sources GO Tau, MWC 480, V892 Tau and DR Tau have lower limits to the temperatures of 30 K and in general suggest high temperatures up to a few hundred Kelvin. Such high temperatures indicate that the upper layers of the disks are heated efficiently by the stellar light and are most probably flared so that they capture the radiation far from the star. Note however that the derived temperatures are extremely sensitive to the errors in the line ratios. DR Tau is surrounded by extended cloud emission and the observed lines may well be emitted in different regions.

In summary, the combined detection of CO 6–5 and H_2 in several sources suggests that these sources may posses a warm upper layer, consistent with a flared disk geometry. Two sources (RY Tau and LkCa 15)

could have lower temperatures on average which could either mean that the disk is flatter, or that dust-settling is taking place, reducing the heating of the gas in the upper layers of the disks (**?**, e.g.)]Chiang01. Higher S/N CO 6–5 data and more accurate calibration are needed to use the 6–5/3–2 ratio as an effective temperature probe (see van Zadelhoff et al. (2001) for a detailed discussion).

5.3. Cold gas masses from CO

Disk masses can be derived from the observed ^{13}CO 3–2 data assuming that most of the flux arises from the outer part of the disk at a constant temperature. The simplification of an isothermal outer disk is supported by detailed modeling along the lines of Beckwith & Sargent (1993). These models have a power-law decrease of the temperature with radius to explain the behavior of the spectral energy distribution, but the gradients in the outer disk are quite small. The reason could be that the ambient interstellar radiation field incident on the outer disk regulates the temperature structure with radius. Because of the large beam dilution, our observations are not sensitive to the warm inner gas, but only probe the outer cold gas. A common outer gas temperature of 30 K is therefore assumed for all our objects. This is slightly higher than the temperature fixed by the local interstellar field, which is around 10–15 K in quiet molecular cloud environments such as found in Taurus and Ophiuchus. It is consistent with the observed ^{13}CO 3–2/1–0 line ratios (van Zadelhoff et al. 2001). In the optically thin limit, the gas mass derived from ^{13}CO 3–2 is given by:

$$M_{\rm gas} = 3 \times 10^{-6} \left(\frac{^{12}[{\rm C}]/[^{13}{\rm C}]}{60}\right) \left(\frac{{\rm H_2}/^{12}{\rm CO}}{10^4}\right) \frac{T_{\rm ex}+0.89}{e^{-16.02/T_{\rm ex}}} \frac{\tau}{1-e^{-\tau}} \left(\frac{d}{100\ {\rm pc}}\right)^2 \int T_{\rm MB}\ dV\ {\rm M}_\odot \qquad (5)$$

The derivation of this formula is similar to that for CO 1–0 by Scoville et al. (1986). The mass varies by a factor of 2 for excitation temperatures between 20 and 100 K, so that the exact value of the excitation temperature is not crucial. Two main parameters must be assumed: the $[^{12}{\rm C}]/[^{13}{\rm C}]$ elemental isotope ratio and the ${\rm H_2}/^{12}{\rm CO}$ conversion factor. This factor is certainly not constant from source to source and we adopt here a reference value of 10^4, typical for dense molecular gas in which CO is not depleted. As will be shown below, this factor is likely to be much larger in disks due to the combined chemical effects of freeze-out and photodissociation.

For sources for which no ^{13}CO data are available (CQ Tau, AA Tau, 49 Ceti, HD 135344), the ^{12}CO data have been used to determine the cold gas masses.

5.4. Cold gas masses from millimeter continuum emission

The cold gas masses can also be determined from the millimeter continuum emission emitted by the cold dust, assuming a gas/dust ratio. All sources in our sample have been previously observed in the millimeter continuum with single-dish telescopes, usually at 1.3 or 1.1 millimeter (**?**, e.g.)]BSCG90,OB95,MS97,MS00,Hen98,WSD89. For some sources, millimeter interferometer data exist at the same wavelengths, giving similar flux levels (Mannings & Sargent 1997), indicating that most of the single-dish emission indeed comes from the disk rather than any remnant envelope. To compute the cold dust mass, $T_{\rm dust} = 30$ K is adopted, similar to that found for CO. The value for the mass absorption coefficient κ_λ (gas + dust) is taken to be $0.01(1.3\,{\rm mm}/\lambda)$ cm^2 g^{-1} from Ossenkopf & Henning (1994) and assumes $M_{\rm gas}/M_{\rm dust} = 100$. The disk mass (gas + dust) is

then given by:

$$M_{\rm disk} = 0.06\ {\rm M}_\odot\ \frac{F_\lambda}{1\ {\rm Jy}} \left(\frac{d}{100\ {\rm pc}}\right)^2 \frac{50\ {\rm K}}{\langle T \rangle} \frac{0.01\ {\rm cm}^2\ {\rm g}^{-1}}{\kappa_{1.3\ {\rm mm}}}, \quad (6)$$

where F_ν is the observed flux at 1.3 mm in Jy. The observational data and resulting masses are summarized in Table 7. The errors in the observed fluxes are taken to be ∼30%.

6. Analysis

6.1. Comparison of derived masses

In the previous section, we applied three methods to estimate the masses of disks around pre-main-sequence and debris-disk stars, summarized in Table 9. The derived masses differ considerably, well beyond the error bars. We now discuss the strengths and weaknesses of each of these methods.

In the upper panel of Figure 10, the masses obtained from the ^{13}CO 3–2 spectra are compared to those computed from the 1.3 millimeter continuum emission assuming a mean disk temperature of 30 K for the T Tauri and Herbig Ae stars. The dust around HD 135344 and β Pictoris has been taken to be warmer at 95 and 85 K respectively (**?**, see)]CW95,Dent00. The results for sources for which only ^{12}CO data are available are included, as well as those for TW Hya studied by van Zadelhoff et al. (2001). As found in previous studies based on lower-J transitions (**?**, e.g.)]Dut96,MS97,MS00, the masses derived from CO are in general factors of 10–200 lower than those found from the millimeter continuum. No distinction can be made between T Tauri and Herbig Ae stars. The debris-disk objects as well as TW Hya seem to suffer very strong CO depletion, more than a factor of 10^3, in agreement with previous studies (**?**, e.g.)]LA98,Dent95. Many explanations have been put forward, including depletion of CO onto grains and dispersal of the disk gas. As argued in §5.1, optical depths effects are unlikely to be the main cause. van Zadelhoff et al. (2001) show that the underabundance of CO is plausibly caused by a combination of freeze-out in the coldest regions of the disk near the mid-plane, as well as photodissociation of CO in the upper layers of the disk by stellar and interstellar ultraviolet radiation (Aikawa et al. 1996; Kamp & Bertoldi 2000; Willacy & Langer 2000). Substantial depletions due to freeze-out have been found in dense, cold molecular cloud cores and in young stellar objects environments (**?**, e.g.)]Kramer99,Shuping01.

The millimeter continuum method is not exempt from difficulties either. In particular, it suffers from the poor knowledge of the dust opacity constants κ_λ. Theoretically, κ_λ should be well determined for particles that are much smaller than the wavelength of observation, but its value depends strongly on the assumed particle composition (silicates, amorphous carbon, ice mantle) and also on particle size, shape and fluffyness. Within the range of possible values, however, κ_λ remains small enough to ensure that the emission is optically thin beyond a few AU, so that the determination of the total mass is quite straightforward. Other assumptions in this method include a constant κ_λ for the whole sample (i.e., no evolution of the opacity constant) and the gas/dust ratio of 100:1 in the disks.

In the lower panel of Figure 10, the warm gas masses derived from the H_2 lines are plotted as functions of the total gas masses obtained from the 1.3 millimeter continuum. For the pre-main sequence stars, the warm gas masses are a fraction (1–10%) of the total gas masses, assuming a gas/dust ratio of 100. Some sources such as LkCa 15, however, show a much larger fraction, of order 30%. Chiang et al. (2001) modeled the Spectral Energy Distribution of LkCa 15 and concluded that this source shows the strongest vertical dust settling. In the case of GO Tau, contamination by surrounding emission is possible. The warm gas

masses have also been plotted versus the cold gas masses derived from ^{13}CO, but no correlation is found, as expected.

6.2. Age determination and evolutionary trends

In order to search for evolutionary trends in our results, the ages of the stars need to be known. This is usually done by comparing the positions of the stars on a Hertzsprung-Russell diagram with theoretical evolutionary tracks. These tracks have many implicit assumptions, however, and give different results depending on the choice of the equations of state, the model used for convection, the opacities, etc. (**?**, see)for a review]CB00. On the observational side, there are also uncertainties in the distance estimates of the sources, the extinction and to what extent the intrinsic luminosity is affected by disk accretion. The precise spectral type of few sources like MWC 480 remains controversial: A4 or A3ep+sh according to Simon, Dutrey & Guilloteau (2000) and Mannings & Sargent (1997) respectively. Moreover, all T Tauri stars exhibit photometric variability, preventing a precise determination of their characteristics. Some stars such as RY Tau and GG Tau are binary systems and thus their stellar characteristics must be corrected.

Although these factors result in significant absolute uncertainties, the relative ages may be less affected. To obtain a consistent set of relative ages, we have re-estimated the ages of the stars in our sample using the recent pre-main-sequence evolutionary models of Siess, Forestini & Bertout (2000), which take the accretion history into account. The results are shown in Figure 11. We take any binary systems to be single stars, so that their ages should be considered rough estimates. The newly evaluated ages are consistent with previous determinations and are listed in Table 8. If the tracks of D'Antona & Mazzitelli (1997) are used, a similar age ordering is obtained. The discrepancies are largest for brown dwarfs and stars younger than 10^6 years. Since our stars have higher mass (>0.5 $M_\odot$) and ages greater than one million years, the differences between the models are not significant. It is not the purpose of this paper to discuss the validity of the different tracks. The errors in our derived ages are of order 1–2 millions years, increasing for the older objects. The ages of the intermediate mass stars are less well determined because their effective temperature and luminosity do not vary significantly over a large range of ages. In particular, the age of β Pictoris is controversial. Recently, Barrado y Navascués et al. (1999) argue that β Pictoris is only (20±10) $\times 10^6$ years old with the error bar reflecting the uncertainties in the isochrones used to derive the age. The young age of β Pictoris is consistent with the view that it is part of a cluster of recent nearby star formation (**?**, e.g.)]ZW00. Whatever its actual age, β Pictoris is the oldest member in our sample.

Figure 12 shows the total disk masses deduced from the three methods plotted against the ages of the stars. No strong evolutionary trend appears but the behavior seems to be similar for the three methods. Figure 13 presents the total warm + cold gas masses derived from the H_2 + CO data relative to the total dust mass derived from the 1.3 millimeter continuum versus age. As discussed in §6.4, only the debris-disk objects show a gas/dust ratio close to 100:1, but this may be coincidental; for the younger objects, a significant amount of cold H_2 is likely present, but is not traced by CO.

Care has to be taken in the interpretation of these data, however. As mentioned before, the choice of objects in our sample is biased toward the higher disk masses and some of the detections are marginal. In fact, so-called weak-line T Tauri stars are surrounded by disks with lower masses (Brandner et al. 2000). This is consistent with the non-detection of H_2 in these objects by Stapelfeldt, Padgett & Brooke (1999). Our data are not sensitive to masses as small as 10^{-4} $M_\odot$ for objects at a distance of 140 pc. Similarly, β Pictoris may be unusual since it is one of the dustiest members of the debris-disk family. Finally, it is

difficult to compare different absolute masses since the mass of the disk at a given time of its evolution likely depends on the initial mass available.

6.3. Heating mechanisms

The derived amount of warm gas is significant and raises the question of the source of heating. Thi et al. (1999a) discussed several possibilities, including photon heating by stellar and interstellar radiation and shock-heating caused by the interaction between a stellar wind and the surface of disks. Here we investigate whether the observed trends provide further clues to the dominant mechanisms. Quantitative discussions and detailed modeling are left for future work.

Since the disks in our sample have negligible accretion onto the star (typically $< 10^{-8}$ $M_\odot$ yr^{-1}), the irradiation of the central object should control, at least partially, the temperature profile of the disks. To study this scenario, we plot in Figure 14 the excitation temperatures derived from the H_2 S(0) and S(1) lines as functions of the effective temperature of the star. Obviously, no significant correlation is found in this figure. We can, however, distinguish three groups: T Tauri, Herbig Ae and debris-disk stars. The T Tauri stars have gas at ∼100 K, whereas their higher mass counterparts are surrounded by gas at 150 K or more. The higher $T_{\rm ex}$ observed in disks around Herbig Ae stars suggests that the harder stellar ultraviolet radiation can be transformed more efficiently into heat for these objects. However, if the number of photons with wavelengths <1100 Å capable of ionizing atomic carbon is also increased, this results in a larger C^+ abundance, increasing the cooling as well. Detailed modeling of the surface heating as a function of radiation field is needed. Note that classical models of photon-dominated-regions (PDRs) do not show any increase of the H_2 excitation temperature versus strength of the incident radiation field for the normal interstellar field typical of a B0 star, even though the surface temperatures increase (**?**, e.g.)]Mario00a. However, the variation of $T_{\rm ex}$ with effective temperature of the star has not yet been modeled.

A link seems to exist between the excitation temperature and the continuum flux at 28 μm normalized at 100 AU (Figure 14*d*). Above a certain threshold, the excitation temperature increases as the continuum flux becomes higher. As a consequence, the warm gas mass drops with continuum flux or $T_{\rm eff}$ because of the steep dependence of the mass on temperature (Eq. (3) and Figure 3) (see Figure 14*a* and 14*b*). Moreover, the fraction of warm gas to the total gas mass around typical A stars like HD 163296 or AB Aur is small compared to that around T Tauri stars.

The role of ultraviolet radiation in heating the surfaces of flared disks is taken into account in recent models by Chiang & Goldreich (1997, 1999), D'Alessio et al. (1998) and Bell et al. (1997). As shown by Thi et al. (1999a), these models fall short of explaining the observed masses of warm H_2 gas by factors of at least a few. It is not yet clear whether this discrepancy is significant, since the same models also fail for normal molecular clouds unless the grain formation rate of H_2 is significantly enhanced (**?**, e.g.)]Harbart00,Li01. The presence of a thin envelope can enhance the scattered stellar radiation and thus also the warming (Natta 1993). At the edges of PDRs, the main heating agent is the photoelectric effect on grains, with small grains and PAHs being particularly effective (Hollenbach & Tielens 1997; Bakes & Tielens 1994). Spaans et al. (1994) investigated the influence of the effective temperature of the central illuminating star on the gas heating efficiency by very small grains (grain radius between 4 and 180 Å) and PAHs. They showed that the efficiency drops only by a factor of 4 from a star at 10000 K to one at 4000 K. Adding the fact that most T Tauri stars exhibit ultraviolet excess and a strong Lyman alpha emission line, the effective heating by low mass stars compared to intermediate mass stars should be similar. The detections of PAHs around AB Aur

(van den Ancker et al. 2000b) and HD 135344 (Coulson, Walther & Dent 1998) suggest that these large molecules can play a role in the heating of the disks, but quantitative models have not yet been performed. The gas can attain higher temperatures than the dust in these layers, consistent with our observations, and its emission can emerge from the surfaces even if the mid-plane is optically thick in the mid-infrared continuum. The efficiency of photoelectric heating decreases significantly, however, if the size of the grains is increased, so the dust size distribution also plays an important factor in this analysis (Kamp & van Zadelhoff 2001).

Alternatively, the line emission can escape through 'holes' or 'gaps' in the disk created by low-mass companion(s), e.g. planets or brown dwarfs (Lubow & Artymowicz 2000). Such gaps could also result in a larger surface area intercepted by the radiation. In any case, the detection of ultraviolet emission from fluorescent H_2 toward other pre-main-sequence stars indicates that ultraviolet radiation plays some role in these systems (Valenti, Johns-Krull & Linsky 2000). Note that this fluorescent H_2 seen in the ultraviolet must arise from much hotter gas, of order 2000 K, probably located in an inner boundary layer close to the star.

Possible heating of H_2 by shocks created by the interaction of a stellar wind with the surface of disks was discussed by Thi et al. (1999a). A significant constraint is however provided by the non-detection of the H_2 S(3) lines in our sources, since shocks tend to populate the high-J H_2 levels as well. Shock models by Burton et al. (1992) give much higher H_2 excitation temperatures than observed, making them less plausible.

6.4. Gas content of debris disks

The most interesting cases are formed by the debris disk objects HD 135344, β Pictoris and 49 Ceti. The disks around these objects are considered gas poor based on CO observations assuming a H_2/CO conversion factor of 10^4 (Thi et al. 2001). For HD 135344 and β Pictoris, two lines are possibly detected (in more than 50% of the spectra obtained by our data reduction procedure), giving a measure of the temperature and the mass with 10% and 55% uncertainty, respectively, if only the standard 30% calibration errors are considered. For 49 Ceti, only the S(0) line is seen, leading to an H_2 mass of $(3.5\pm1.9)\times10^{-3}$ $M_\odot$ if $T_{\rm ex} = 100$ K is assumed. The derived mass of gas around β Pictoris is $\sim 10^{-4}$ $M_\odot$ or $\sim 0.17\pm0.09$ M_J, and it is $\sim 6.4\ 10^{-3}$ $M_\odot$ around HD 135344. The amount of gas in the β Pictoris disk is significantly smaller than that for other disks. The disks are not resolved within the ISO-SWS beam for HD 135344 and 49 Ceti and barely resolved for β Pictoris. Therefore, the location of the emitting gas is unknown.

The detection of H_2 gas in the β Pictoris disk may seem surprising since this disk has a very low CO/dust mass ratio (**?**, e.g.)]LA98, Zuc95, Roberge00. The presence of some neutral gas was, however, invoked by Lagrange et al. (1998) in order to slow down ions like Ca II or Fe II leaving the disk since these ions suffer strong radiation pressure from the star. They considered only H I as a major species of the stable ring. The detection of Fe II lines together with the measured Fe I/Fe II ratio implies densities of 10^3–10^6 cm^{-3} (Lagrange et al. 1995). This is consistent with the density at 40 AU in the disk model of Kamp & Bertoldi (2000) which has $M_{\rm disk} \sim 10^{-4}$ $M_\odot$, similar to that found here. In their model of debris disks, Kamp & Bertoldi (2000) consider the balance of the formation and destruction of CO and H_2. Their main conclusion is that the CO molecule can exist only in the dense part of disks protected from photodissociation whereas H_2 is widely spread. Moreover, CO freezes out onto dust in the coldest parts near the midplane, making it a poor tracer of the gas.

If the H_2 detections are valid, nearly all of the gas is at high temperatures ($\sim 80 - 100$ K) in the debris

disks. Since the disk of β Pictoris has an optical depth less than unity at optical wavelengths, the ultraviolet photons can warm the gas in the entire disk through the photoelectric effect and other processes (Kamp & van Zadelhoff 2001). These gas temperatures are only slightly higher than those derived for the dust components: the spectral energy distributions of β Pictoris and HD 135344 are well fitted by a single dust temperature of 80–90 K (Walker & Heinrichsen 2000; Coulson & Walther 1995), indicating that these disks are globally warmer than those around T Tauri or Herbig Ae stars.

The estimated total dust mass around β Pictoris ranges from 0.3×10^{-6} $M_\odot$ (Walker & Heinrichsen 2000) to 10^{-6} $M_\odot$ (Li & Greenberg 1998). The gas-to-dust mass ratio lies therefore between 45 and 380, and is much higher than the value of 0.02 derived from CO ultraviolet observations. Note that if these CO molecules are the evaporation products of infalling comets onto β Pictoris (Lecavalier et al. 1996), it is not possible to derive the primordial H_2 content of the disk from CO.

A pertinent consequence of the presence of gas in debris disks is that it affects the dynamics of the dust in those disks (**?**, e.g.)]W77. For sufficiently large gas masses, dust generation by collisions of planetesimals will not be possible. For β Pictoris, however, the gas mass of ~ 0.1 M_J is small enough that it does not prevent a collisional cascade. Takeuchi & Artymowicz (2001) modeled the evolution of dust grains in disks with gas masses up to a few tens of Earth masses, comparable to that found for β Pictoris. They show that although grains migrate radially due to radiative pressure and gravity, equilibrium orbits exist for a specific range of grain sizes. Most interestingly, their models can reproduce ring-like disk morphologies with an inner disk clear of small grains. The similarity of our derived gas/dust ratio for β Pictoris with the interstellar value of ∼100:1 is therefore likely coincidental: some of the dust and gas may have accumulated into (gaseous) planets and planetesimals, been expelled from the disk due to radiation pressure, or fallen onto the star by Poynting-Robertson drag.

7. Conclusions

We have conducted the first survey of H_2 rotational line emission from disks around a sample of T Tauri and Herbig Ae stars and from young stars with debris disk using the ISO-SWS. The observed spectra reveal the presence of an unexpectedly large amount ($0.1–10 \times 10^{-3}$ $M_\odot$) of molecular gas at ∼100 K. No correlations between the warm gas masses with disk masses derived from ^{13}CO and 1.3 millimeter emission were found. Whereas the bulk of the gas around T Tauri and Herbig Ae stars is cold, the warm gas may constitute the major gaseous component of debris-disk objects like HD 135344 and β Pictoris. There is no apparent difference between the low and the intermediate mass pre-main-sequence stars. The possible heating mechanisms responsible for the warm gas are discussed. No process can adequately explain the large amount of warm gas, but the ubiquitous presence of warm H_2, the higher gas than dust temperatures, and the detection of PAHs in few of the objects suggest that a common mechanism like photoelectric heating by ultraviolet radiation could be the main heating agent. Further modeling is needed.

Complementary observations of ^{12}CO 3–2, 6–5 and ^{13}CO 3–2 have been performed. The line profiles are resolved and exhibit double-peaked features consistent with gas emitted from a disk in Keplerian rotation around a central object. Ratios of integrated fluxes of the two isotopomers ^{12}CO and ^{13}CO show that the ^{13}CO 3–2 line is not highly optically thick and potentially a tracer of the cold component of disks. The presence of warm gas is supported by the detection of ^{12}CO 6–5 toward a few sources where H_2 has also been found. The gaseous masses inferred from the ^{13}CO intensities are much smaller than those found from the dust continuum emission. CO is likely strongly affected by photodissociation via the stellar and interstellar

ultraviolet radiation in the surface layers and freeze-out onto grain surfaces in the midplane.

The H_2, CO and millimeter continuum data together with rough age estimates of our stars allow evolutionary trends to be investigated. No strong evolution in the masses derived from CO, H_2 or dust is found. There is a large diversity among the stars studied in the $(1–10)\times10^6$ years range. The limited number of objects, the limited quality of the ISO data and uncertainties in the derived masses prevent definitive conclusions on the gas survival time scale.

The analysis of the H_2 data presented here suffers greatly from limited spatial and spectral resolution as well as sensitivity. Ground-based spectrometers soon to be operational on 8–10 m class telescopes will be able to study the S(1) line at vastly higher spectral and spatial resolution, but will not have access to the ground state para-H_2 transition at 28 μm. Moreover, the surface brightness sensitivities of these warm large telescopes is only marginally improved compared with small cryogenic space observatories such as ISO. More complete studies with future air- and space-borne mid-infrared spectrometers on SIRTF, SOFIA, and eventually NGST will greatly improve on our ability to examine the H_2 emission lines from young stars, and properly address the many interesting questions associated with the structure of circumstellar disks and the formation of giant gaseous planets raised in this paper.

This work was supported by the Netherlands Organization for Scientific Research (NWO) grant 614.41.003 and a Spinoza grant , and by grants to GAB from NASA (NAG5–8822 and NAG5–9434). A.N. is supported in part by ASI ARS-98-116 grant. Discussions with Eugene Chiang, Peter Goldreich, Michiel Hogerheijde, Frank Shu and Doug Johnstone are appreciated. The authors thank the staff of the CSO and JCMT, in particular Fred Baas and Remo Tilanus, for their support and the Dutch ISO Data Analysis Center (DIDAC) at SRON-Groningen, especially Edwin Valentijn and Fred Lahuis, for their help during the data reduction of the ISO-SWS spectra.

REFERENCES

Adams, F. C., Lada, C. J., & Shu, F. H. 1987, ApJ, 312, 788

Aikawa, Y., Miyama, S., Nakano, T., & Umebayashi, T. 1996, ApJ, 467, 684

Backman, D. E., & Paresce, F. 1993, in Protostars and Planets III, eds. E. H. Levy & J. Lunine (Tucson: Univ. Arizona Press), 1253

Bakes, E. L. O., & Tielens, A. G. G. M. 1994, ApJ, 427, 822

Barrado y Navascués, D., Stauffer, J. R., Song, I., & Caillault, J.-P. 1999, ApJ, 520, 123

Beckwith, S. V. W., Sargent, A. I., Chini, R. S., & Guesten, R. 1990, AJ, 99, 924

Beckwith, S. V. W., & Sargent, A. I. 1996, Nature, 383, 189

Beckwith, S. V. W., & Sargent, A. I. 1993, ApJ, 402, 280

Bell, K. R., Cassen, P. M., Klahr, H. H., & Henning, Th. 1997, ApJ, 486, 372

Berrilli, F., Corciulo, G., Ingrosso, G., Lorenzetti, D., Nisini, B., & Strafella, F. 1992, ApJ, 398, 254

Bertout, C., Robichon, N., & Arenou, F. 1999, A&A, 352, 574

Bockelée-Morvan, et al. 1995, in Circumstellar Dust Disks & Planet Formation, eds. R. Ferlet & A. Vidal-Madjar, Editions Frontières, Gif sur Yvette,

Bodenheimer, P., Hubickyj, O., & Lissauer, J. 2000, Icarus, 143, 2

Bouwman, J., de Koter, A., van den Ancker, & M. E., Waters, L. B. F. M. 2000, A&A, 360, 213

Brandner, W., et al. 2000, AJ, 120, 950

Burton, M. G., Hollenbach, D. J., & Tielens, A. G. G. M. 1992, ApJ, 399, 563

Butler, R. P., et al. 1999, ApJ, 526, 916

Calvet, N., Patino, A., Magris, G. C., D'Alessio, P. 1991, ApJ, 380, 617

Chabrier G., & Baraffe I. 2000, ARA&A, 38, 337

Charbonneau, D., Brown, T. M., Latham, D. W., & Mayor, M. 2000, ApJ, 529, 45

Chiang, E. I., & Goldreich, P. 1997, ApJ, 490, 368

Chiang, E. I., & Goldreich, P. 1999, ApJ, 519, 279

Chiang, E. I., Joung, M. K., Creech-Eakman, M. J., Qi, C., Kessler, J. E., Blake, G. A., & van Dishoeck, E. F. 2001, ApJ, 547, 1077

Chini, R., Krügel, E., Shustov, B., Tutukov, A., & Kreysa, E. 1991, A&A, 252, 220

Coulson, I. M., Walther, D. M., & Dent, W. R. F. 1998, MNRAS, 296, 934

Coulson, I. M., & Walther, D. M. 1995, MNRAS, 274, 977

Crifo, F., Vidal-Madjar, A., Lallement, R., Ferlet, R., & Gerbaldi, M. 1997, A&A, 320, L29

D'Alessio, P., Cantó, J., Calvet, N., & Lizano, S. 1998, ApJ, 500, 411

D'Antona, F., & Mazzitelli, I. 1997 , in Cool stars in Clusters & Associations, eds. G. Micela & R. Pallavicini, Mem. S.A.It., 68, 807

de Graauw, Th., et al. 1996, A&A, 315, L49

Dent, W. R. F., Walker, H. J., Holland, W. S., & Greaves, J. S. 2000, MNRAS, 314, 702

Dent, W. R. F., Greaves, J. S., Mannings, V., Coulson, I. M., & Walther, D. M. 1995, MNRAS, 277, L25

Dunkin, S. K., Barlow, M. J., & Ryan, S. G. 1997, MNRAS, 286, 604

Dutrey, A., Guilloteau, S., Duvert, G., Prato, L., Simon, M., Schuster, K., & Menard, F. 1996, A&A, 309, 493

Dutrey, A., Guilloteau, S., & Guélin, M. 1997, 317, A&A, L55

Dutrey, A., Guilloteau, S., Prato, L., Simon, M., Duvert, G., Schuster, K., Menard, F. 1998, A&A, 338, L63

Elmegreen, B. G. 1978, Moon & Planets, 19, 159

Elmegreen, B. G. 1979, A&A, 80, 77

Flower, D.R. 1998, MNRAS, 297, 334

Friedemann, C., Riemann, H. G., Gürtler, J., & Tóth, V. 1993, ApJ, 277, 184

Freudling, W., Lagrange, A. M., Vidal-Madjar, A., Ferlet, R., & Forveille, T. 1995, A&A, 301, 231

Ghez, A. M., White, R. J., & Simon, M. 1997, ApJ, 490, 353

Gredel, R., van Dishoeck, E. F., & Black, J. H. 1994, A&A, 285,300

Guilloteau, S., Dutrey, A., & Simon, M. 1999, A&A, 348 570

Guillot T. 1999, Science, 286, 72

Habart, E., Boulanger, F., Verstraete, L., Falgarone, E., Pineau Des Forêts, G., & Abergel, A. 2000, in ISO beyond the peaks: The 2nd ISO workshop on analytical spectroscopy, held 2-4 February 2000, at VILSPA., 103

Haisch K. E. Jr, Lada, E. A., Lada, Ch. J. 2001, ApJ, 553, 153

Hartmann, L., Calvet, N., Gullbring, E., & D'Alessio, P. 1998, ApJ, 495, 385

Heap, S. R., Lindler, D. J., Lanz, Th. M., Cornett, R. H., & Hubeny I. 2000, ApJ, 539, 435

Henning, Th., Burkert, A., Launhardt, R., Leinert, C., & Stecklum, B. 1998, A&A, 336, 565

Henning, Th., Launhardt, R., Steinacker, J., & Thamm, E. 1994, A&A, 291, 546

Hollenbach, D. J., & Tielens, A. G. G. M. 1997, ARA&A, 35, 179

Hollenbach, D. J., Yorke H. W., & Johnstone, D. 2000, in Protostars and Planets IV, eds. V. Mannings, A. P. Boss & S. S. Russell (Tucson: Univ. Arizona Press), 401

Horedt, G.P. 1982, A&A, 110, 209

Jennings, D. E., Weber, A., & Brault, J. W. 1987, J. Mol. Spectroc., 126, 19

Kamp, I., & Bertoldi, F. 2000, A&A, 353, 276

Kamp, I., & van Zadelhoff, G.-J. 2001, A&A, in press

Kenyon, S. J., Dobrzycka, D., & Hartmann, L. 1994, ApJ, 108, 1872

Kenyon, S. J., & Hartmann, L. 1995, ApJS, 101, 117

Kenyon, S. J., & Hartmann, L. 1987, ApJ, 323, 714

Klahr, H. H., & Lin, D. N. C., 2001, AJ, in press

Koerner, D. 2000, in Astrochemistry: from Molecular Clouds to Planetary Systems, IAU Symposium 197, eds. Y. C. Minh & E. F. van Dishoeck (San Francisco: ASP), 393

Koerner, D. W., & Sargent, A. I. 1995, AJ, 109, 2138

Kooi, J. W., Schaffer, P. L., Bumble, B., et al. 1998, SPIE, 3357, 22

Kramer C., Alves, J., Lada, C. J., et al. 1999, A&A, 342, 257

Lagrange, A.-M., et al. 1995, A&A, 296, 499

Lagrange, A. M., Beust, H., Mouillet, D., Emerich, C., Beust, H., & Ferlet, R.. 1998, A&A, 329, 1028

Lagrange, A.-M., Backman, D. E., & Artymowicz, P. 2000, in Protostars and Planets IV, eds. V. Mannings, A. P. Boss & S. S. Russell (Tucson: Univ. Arizona Press), 639

Lecavalier de Etangs, A., Vidal-Madjar, A., & Ferlet, R. 1996, A&A, 307, 542

Li, A., & Greenberg, J.M. 1998, A&A, 291, 313

Li, W., Evans, N.J., Jaffe, D.T., van Dishoeck, E.F., & Thi, W.F. 2001, ApJ, to be submitted

Lin, D. N. C., Papaloizou, J. C. B., Terquem, C., Bryden, G., & Ida, S. 2000, in Protostars and Planets IV, eds. V. Mannings, A. P. Boss & S. S. Russell (Tucson: Univ. Arizona Press), 1111

Liseau, R., & Artymozicz, P. 1998, A&A, 334, L935

Lissauer, J. 1993, ARA&A, 31, 129

Lubow, S. H., & Artymozicz, P. 2000, in Protostars and Planets IV, eds. V. Mannings, A. P. Boss & S. S. Russell (Tucson: Univ. Arizona Press), 731

Mannings, V., & Sargent, A. I. 2000, ApJ, 529, 391

Mannings, V., & Sargent, A. I. 1997, ApJ, 490, 792

Mannings, V., & Emerson, J. P. 1994, MNRAS, 267, 361

Marcy, G. W., Cochran, W. D., & Mayor, M. 2000, in Protostars & Planets IV (Tucson: University of Arizona), eds. V.G. Mannings, A.P. Boss, & S.S. Russell, 1285

Men'shchikov, A. B., Henning, Th., & Fischer, O. 1999, ApJ, 519, 257

Miyake, K., & Nakagawa, Y. 1995, ApJ, 441, 361

Natta, A., et al. 2001, A&A, in press

Natta, A., Grinin, V. P., & Mannings V. 2000, in Protostars & Planets IV, eds. V. Mannings, A. P. Boss & S. S. Russell (Tucson: Univ. Arizona Press), 559

Natta, A., et al. 1999, A&A, 350, 541

Natta, A., Grinin, V. P., Mannings, V., & Ungerechts, H. 1997, ApJ, 491, 885

Natta, A. 1993, ApJ, 412, 761

Ossenkopf, V., & Henning, Th. 1994, A&A, 279, 577

Osterloh, M., & Beckwith, S. V. W. 1995, ApJ, 439, 2880

Reach, W. T., et al. 1996, A&A, 315, L381

Roberge, A., et al. 2001, ApJ, 551, L97

Roberge, A., et al. 2000, ApJ, 904

Ruden, S. P. 1999, in The Origin of Stars & Planetary Systems, eds. C. J. Lada & N. D. Kylafis (Dordrecht: Kluwer), 643

Sandford, S. A., & Allamandola, L. J. 1993, ApJ, 409, 65

Scoville, N. Z., Sanders, D. B., Sargent, A. I., Soifer, B. T., Scott, S. L., & Lo, K. Y. 1986, ApJ, 303, 416

Shuping, R. Y., Chiar, J. E., Snow, Th. P., & Kerr, Th. 2001, ApJ, 547, 161

Siess, L., Forestini, M., & Bertout, C. 2000, A&A, 358, 593

Siess, L., Forestini, M., & Bertout, C. 1999, A&A, 342, 480

Simon, M., Dutrey, A., & Guilloteau, S. 2000, ApJ, 545, 1034

Shu, F. H., Johnstone, D., & Hollenbach, D. 1993, Icarus, 106, 92

Shull, J. M., et al. 2000, ApJ, 538, L73

Snow, T. P. , et al. 2000, ApJ, 538, L65

Spaans, M., Tielens, A. G. G. M., van Dishoeck, E. F., & Bakes, E. L. O. 1994, ApJ, 437, 270

Spitzer, L. Jr., & Jenkins, L. B. 1975, ARA&A, 13, 133

Stapelfeldt, K., Padgett, D., & Brooke, T. Y. 1999, in The Universe as viewed by ISO, eds. P. Cox & M.F. Kessler, ESA-SP 427 (Noordwijk: ESTEC), p. 525

Strom, K. M., Wilking, F. P., Strom, S. E., & Seaman, R. L. 1989, AJ, 98, 1444

Sylvester, R. J., Skinner, C. J., Barlow, M. J. 1997, MNRAS, 289, 831

Sylvester, R. J., Skinner, C. J., Barlow, M. J., & Mannings V. 1996, MNRAS, 279, 915

Takeuchi, T., & Artymowicz P. 2001, ApJ, submitted

Thi, W. F., et al. 1999a, ApJ, 521, 63

Thi, W. F., et al. 1999b, in The Universe as viewed by ISO, eds. P. Cox & M.F. Kessler, ESA-SP 427 (Noordwijk: ESTEC), p. 529

Thi, W. F., et al. 1999c, in The Universe as viewed by ISO, eds. P. Cox & M.F. Kessler, ESA-SP 427 (Noordwijk: ESTEC), p. 767

Thi, W. F., et al. 2001, Nature, 409, 60

Valenti, J. A., Johns-Krull, C. M., & Linsky J. L. 2000, ApJS, 129, (Jul 2000)

Valentijn, E. A., & Thi, W.F. 2000, Experimental Astronomy, 10, 215

van den Ancker, M. E., Tielens, A. G. G. M., & Wesselius, P. R. 2000a, A&A, 358, 1035

van den Ancker, M. E., Bouwman, J., Wesselius, P. R., Waters, L. B. F. M., Dougherty, S. M., van Dishoeck, E. F. 2000b, A&A, 357, 325

van den Ancker, M. E., The, P. S., Tjin A Djie, H. R. E., Catala, C., de Winter, D., Blondel, P. F. C., & Waters, L. B. F. M. 1997, A&A, 324, L33

van Dishoeck, E. F., et al. 1998, Ap&SS, 255, 77

van Dishoeck, E. F., Phillips, T. G., Black, J. H., & Gredel, R. 1991, ApJ, 366, 141

van Zadelhoff, G.-J., van Dishoeck, E. F., Thi, W. F., & Blake, G. A. 2001, A&A, submitted

Walker, H. J., & Heinrichsen, I. 2000, Icarus, 143, 147

Webb, R. A., et al. 1999, ApJ, 512, 63

Weidenschilling, S. J. 1977, MNRAS, 180, 57

Weintraub, D. A., Kastner J. H., & Bary, J. S. 2001, ApJ, 541, 767

Weintraub, D. A., Sandell, G., & Duncan, W. D. 1989, ApJ, 340, 69

Wichmann, R., Bastian, U., Krautter, J., Jankovics, I., & Ruciński, S. M. 1999, MNRAS, 301, 39

Willacy K., & Langer, W. D. 2000, ApJ, 544, 903

Wolniewicz, L., Simbotin, I., & Dalgarno, A. 1998, ApJS, 115, 293

Zuckerman, B., Forveille, T., & Kastner, J. H. 1995, Nature, 373, 494

Zuckerman, B., & Webb, R. A. 2000, ApJ, 535, 959

AAS LaTeX macros v5.0.

Table 1. Stellar characteristics

Name	SpT	α(J2000)	δ(J2000)	$\log(T_{\rm eff})$	$\log(L_*/L_\odot)$	d[a](pc)	Ref.
			T Tauri stars				
AA Tau	K7	04 34 55.5	+24 28 54	3.60	−0.15	140	1
DM Tau	M0.5	04 33 48.7	+18 10 12	3.56	−0.5	140	1
DR Tau	K7	04 47 06.3	+16 58 41	3.64	+0.025	140	2
GG Tau[b]	K7	04 32 30.3	+17 31 41.0	3.58	−0.22 ±0.23	140	3
GO Tau	M0	04 43 03.1	+25 20 19	3.58	−0.43	140	1
RY Tau[c]	K1	04 21 57.41	+28 26 35.6	3.76	+0.81	133	2, 4
GM Aur	K7	04 55 10.2	+30 21 58	3.59	−0.12	140	2
LkCa 15	K7	04 39 17.8	+22 21 03	3.64	−0.27	140	2
			Herbig Ae stars				
UX Ori	A3IIIe	05 04 29.9	−03 47 14.3	3.94	$+1.51\ ^{+0.15}_{-0.13}$	430	7
HD 163296	A3Ve	17 56 21.26	−21 57 19.5	3.94	+1.41 ±0.69	$122\ ^{+17}_{-13}$	8
CQ Tau	F5IVe	05 35 58.47	+24 44 54.1	3.84	$-0.21\ ^{+0.19}_{-0.16}$	$100\ ^{+25}_{-17}$	8
MWC 480	A3ep+sh	04 58 46.27	+29 50 37.0	3.94	$+1.51\ ^{+0.15}_{-0.13}$	$131\ ^{+24}_{-18}$	8
MWC 863	A1Ve	16 40 17.92	−23 53 45.2	3.97	$+1.47\ ^{+0.25}_{-0.19}$	$150\ ^{+40}_{-30}$	8
HD 36112	A5IVe	05 30 27.53	+25 19 57.1	3.91	$+1.35\ ^{+0.24}_{-0.18}$	$200\ ^{+60}_{-40}$	7
AB Aur	A0Ve+sh	04 55 45.79	+30 33 05.5	4.00	$+1.68\ ^{+0.13}_{-0.11}$	$144\ ^{+23}_{-17}$	8
WW Vul	A0	19 25 58.75	+21 12 31.3	3.97	+0.73	550	9
V892 Tau	A0	04 18 40.61	+28 19 16.7	3.90	+1.75	140	10
			Debris-disk stars				
49 Ceti	A1V	01 34 37.78	−15 40 34.9	3.97	+1.37	61	11
HD 135344	F8V	15 15 48.44	−37 09 16.0	3.79	+0.60	80	12
β Pictoris	A5V	05 47 17.09	−51 03 59.5	3.91	+0.94	19.28 ±0.19	13

[a]In cases where no accurate (Hipparcos) distance is available, a mean distance of 140 pc is adopted (Kenyon, Dobrzycka & Hartmann 1994).

[b]Characteristics of the most massive star of the binary system.

[c]Possible binary system (Bertout, Robichon & Arenou 1999).

References. — (1) Hartmann et al. 1998; (2) Siess, Forestini & Bertout 1999; (3) Ghez et al. 1997; (4) Wichmann et al. 1998; (5) Kenyon & Hartmann 1995; (6) Webb et al. 1999; (7) Natta et al. 1999; (8) van den Ancker et al. 1997; (9) Friedemann et al. 1993; (10) Berrilli et al. 1992; (11) Coulson, Walther & Dent 1998; (12) Coulson & Walther 1995 (13) Crifo et al. 1997; (14) Mannings & Sargent 1997

Table 2. H_2 molecular line data

Transition	Wavelength[a] (μm)	$E_{\rm upper}$[a] (K)	A–coefficient[b] (s^{-1})	$n_{\rm crit}$[c] at 100 K (cm^{-3})
H_2 S(0) 2→0	28.218	509.88	$2.94\ 10^{-11}$	54
H_2 S(1) 3→1	17.035	1015.12	$4.76\ 10^{-10}$	$1.1\ 10^{3}$
H_2 S(2) 4→2	12.278	1814.43	$2.76\ 10^{-9}$	$2.0\ 10^{4}$
H_2 S(3) 5→3	9.662	2503.82	$9.84\ 10^{-9}$	$1.9\ 10^{5}$

References. — (a) Jennings et al. 1987; (b) Wolniewicz et al. 1998; (c) using H_2–H_2 collisional transition rate coefficients from Flower (1998).

Table 3. H_2 integrated fluxes with inferred temperature and mass

Name	H_2 S(0) (10^{-14} erg s^{-1} cm^{-2})	H_2 S(1) (10^{-14} erg s^{-1} cm^{-2})	T_{ex} (K)	H_2 mass (10^{-3} $M_\odot$)	Level of confidence
AA Tau	<1.5	8.1±0.25	100–200[a]	20.6–0.2	medium
DR Tau	<1.5	<0.8	···	···	···
GG Tau	2.5±0.8	2.8±0.8	110±11	3.6±1.8	high
GO Tau	5.6±1.7	7.1±2.1	113±11	6.4±3.2	medium
RY Tau	<1.5	<0.8	···	···	···
GM Aur	<1.5	<0.8	···	···	···
LkCa 15	5.7±2.2	5.3±1.6	105±10	8.6±4.3	medium
UX Ori	6.8±2.0	<0.8	100–200[a]	117–9	high
HD 163296	1.9±0.6	22±6	220±22	0.4±0.2	high
CQ Tau	5.9±1.8	40±12	180±18	2.0±1.0	high
MWC 480	<1.5	10±3	100–200[a]	78.8–0.7	···
MWC 863	6.9±2.1	24±7	146±14	1.5±0.8	high
HD 36112	<1.5	3.6±1.1	100–200[a]	18.7–0.2	medium
AB Aur	4.1±1.2	30±9	185±18	1.3±0.7	high
WW Vul	<1.5	<0.8	···	···	···
49 Ceti	6.6±2.0	<0.8	100–200[a]	2.3–0.3	medium
HD 135344	9.0±2.7	5.5±1.7	97±10	6.4±3.2	medium
β Pictoris	7.0±2.1	7.7±2.3	109±11	0.17±0.08	medium

[a]Assumed temperature range

Note. — All upper limits are 3σ. No correction for extinction has been taken into account in the calculation of the temperatures and masses. The errors on the fluxes of ∼30% translate into uncertainties of ∼10 % on the temperatures and ∼55% on the mass. The level of confidence of the detection is considered "high" when the line is detected in more than 75% of the 1000 reduced spectra. The level becomes "medium" when the detection is present in about 50–75% of the spectra. In cases of non-detection, the line is seen in less than 50% of the reductions.

Table 4. Observed continuum fluxes near H_2 lines

Name	3.4 μm (Jy)	6.9 μm (Jy)	9.6 μm (Jy)	17 μm (Jy)	28.2 μm (Jy)	$T_{\rm thin}$ (K)	Remarks
AA Tau	<0.1	<0.1	0.1	1.1	1.2	93±9	[a]
DR Tau	2.0	1.7	2.4	4.3	5.4	90±9	
GG Tau	0.5	0.4	0.8	1.1	2.1	81±8	[a]
GO Tau	0.2	0.2	0.3	<0.1	1.4	88±9	[a]
RY Tau	5.2	5.1	15.9	17.0	16.9	92±9	
GM Aur	<0.1	<0.1	0.5	0.1	1.2	56±6	[a]
LkCa 15	0.3	0.4	0.5	0.4	0.2	120±12	[a]
UX Ori	1.0	0.7	3.5	1.4	4.6	71±7	
HD 163296	8.5	7.0	18.0	16.9	15.4	78±8	
CQ Tau	2.6	2.1	7.1	13.1	21.6	155±15	
MWC 480	3.8	3.7	8.7	4.7	7.2	85±9	
MWC 863	6.1	5.5	22.3	16.7	16.2	98±10	
HD 36112	3.6	2.5	6.3	4.8	6.4	81±8	
AB Aur	13.2	9.6	29.9	24.4	45.4	96±10	
WW Vul	0.9	0.7	2.3	1.8	2.1	84±8	
49 Ceti	1.8	0.6	0.3	0.8	0.2	161±16	[a]
HD 135344	3.2	2.1	1.3	2.8	8.0	74±7	
β Pictoris	12.4	3.4	2.7	3.0	6.6	96 ±10	

Note. — Photometric errors are $\sim$ 30% and the errors on the derived temperatures are $\sim$10%.

[a]Strongly dominated by the zodiacal light emission, which is $\sim$0.3 Jy at mid-infrared wavelengths.

Table 5. CO J=3–2 observations on source

Name	^{12}CO 3–2			^{13}CO 3–2				
	$\int T_{\rm MB} dV$ (K km s^{-1})	$V_{\rm LSR}$ (km s^{-1})	ΔV (km s^{-1})	$\int T_{\rm MB} dV$ (K km s^{-1})	$V_{\rm LSR}$ (km s^{-1})	ΔV (km s^{-1})	$\bar{\tau}$[a]	$M_{\rm disk}(^{13}{\rm CO})$ (10^{-3} M$_\odot$)
DM Tau	1.02±0.30	6.2	1.0	0.25±0.07	6.4	0.6	0.56	0.18±0.05
	···	···	···	0.19±0.06	5.6	0.6	···	···
DR Tau	3.45±1.03	6.8	0.7	0.21±0.06	6.9	0.3	0.06	0.07±0.02
	1.93±0.58	9.1	0.5	···	···	···	···	···
	6.84±2.05[c]	10.3	1.0	···	···	···	···	···
	1.38±0.41[c]	10.0	0.9	···	···	···	···	···
GG Tau	1.28±0.38	5.7	1.0	0.21±0.06	5.5	1.2	0.19	0.16±0.05
	1.41±0.42	7.0	1.0	0.27±0.08	7.2	1.2	···	···
GO Tau	0.77±0.23	5.2	1.0	0.11±0.03	4.3	0.8	0.18	0.09±0.03
	1.31±0.39	7.1	1.0	0.09±0.03	7.0	0.3	···	···
	0.18±0.05[c]	6.2	0.4	···	···	···	···	···
	0.09±0.03[c]	5.5	0.7	···	···	···	···	···
RY Tau	3.94±1.18	6.3	0.3	0.21±0.06	6.4	0.3	···	0.06±0.02
	2.48±0.74	6.9	0.3	···	···	···	···	
GM Aur	0.62±0.18	4.8	1.0	0.24±0.07	4.6	1.6	0.35	0.16±0.05
	0.89±0.27	6.4	0.9	0.21±0.06	6.9	1.5	···	···
LkCa 15	0.58±0.17	5.4	1.3	0.16±0.05	5.2	1.4	0.38	0.14±0.04
	0.61±0.18	7.0	1.3	0.22±0.06	7.1	1.4	···	···
HD 163296	1.44±0.43	4.7	1.5	0.43±0.13	4.5	1.5	0.62	0.56±0.16
	1.63±0.49	6.9	1.5	0.51±0.15	7.3	1.5	···	···
	0.75±0.22 [c]	5.5	7.0	···	···	···	···	
	0.83±0.25 [c]	5.5	7.0	···	···	···	···	···
CQ Tau	< 0.06	···	···	< 0.06[b]	···	···	···	···
MWC 480	1.25±0.37	4.2	1.1	0.27±0.08	4.0	1.2	0.27	0.17±0.05
	1.12±0.33	6.0	1.1	0.30±0.09	6.2	1.2	···	
HD 36112	1.03±0.31	4.9	4.7	0.31±0.09	5.9	1.8	0.36	0.23±0.07
AB Aur	26.1±7.8	5.8	1.5	5.00±1.50	5.8	1.6	0.21	1.72±0.51
V892 Tau	2.18±0.65	7.0	1.1	···	···	···	···	···
	2.27±0.68	8.2	1.2	···	···	···	···	···
HD 135344	0.39±0.12	6.4	1.0	···	···	···	···	2.1±0.6×10^{-3} [d]
	0.41±0.12	7.7	1.0	···	···	···	···	···

Table 5—Continued

	^{12}CO 3–2			^{13}CO 3–2				
Name	$\int T_{\rm MB} dV$ (K km s^{-1})	$V_{\rm LSR}$ (km s^{-1})	ΔV (km s^{-1})	$\int T_{\rm MB} dV$ (K km s^{-1})	$V_{\rm LSR}$ (km s^{-1})	ΔV (km s^{-1})	$\bar{\tau}$[a]	$M_{\rm disk}(^{13}{\rm CO})$ (10^{-3} M$_\odot$)

[a]Beam-averaged optical depth of ^{13}CO line from ^{12}CO/^{13}CO ratio, assuming $T_{\rm ex}(^{12}{\rm CO})$=$T_{\rm ex}(^{13}{\rm CO})$.

[b]No line detected; the 3σ upper limit is computed by assuming a total line width of 3 km s^{-1}.

[c]Extended cloud emission

[d]Mass computed from ^{12}CO 3–2 emission.

Table 6. ^{12}CO 6–5 line parameters.

Name	$\int T_{\rm MB} dV$ (K km s^{-1})	$V_{\rm LSR}$ (km s^{-1})	ΔV (km s^{-1})
DL Tau	<1.8	···	···
DM Tau	<1.8	···	···
DR Tau	11.6±1.5	10.0	1.6
GG Tau	1.9±0.4	4.9	3.5
GO Tau	4.7±1.3	5.2	2.4
RY Tau	<2.0	···	···
GM Aur	2.8±0.7	5.1	1.6
LkCa 15	1.9±0.8	6.8	3.3
CQ Tau	<2.8	···	···
MWC 480	2.3±0.8	4.9	2.5
AB Aur	51.7±2.2	5.9	2.1
V892 Tau	11.7±0.7	7.4	1.2

Note. — 3σ upper limits computed assuming a line width ΔV=3 km s^{-1}.

Table 7. Disk mass deduced from 1.3mm flux.

Name	$M_{\rm disk}$[a] (10^{-2}M$_\odot$)	F$_{1.3mm}$ (mJy)	Ref.
AA Tau	1.7±0.8	88±26	1
DM Tau	2.1±0.9	109±33	1
DR Tau	3.1±1.4	159±48	1
GG Tau	11.6±5.2	593±178	2
GO Tau	1.6±0.7	83±25	1
RY Tau	4.0±1.8	229±69	1
GM Aur	4.9±2.2	253±76	1
LkCa 15	3.3±1.5	167±50	3
TW Hya	1.5±0.7	784±235 [b]	4
UX Ori	4.2±1.9	23±7	6
HD 163296	6.5±2.9	441±132	7
CQ Tau	2.2±1.0	221±66	7
MWC 480	2.2±1.0	131±39	7
MWC 863	1.0±0.5	45±13	7
HD 36112	2.9±1.3	72±21	7
AB Aur	2.1±0.9	100±30	8
WW Vul	3.2±1.4	10.5±3.1	9
V892 Tau	5.6±2.5	289±87	8
49 Ceti	0.04±0.018	12.7±3.8	10
HD 135344	0.28±0.126	142±42	11
β Pictoris	0.003±0.00135	24±7	12

[a]Assuming a dust temperature of 30 K except for HD 135344 and β Pictoris for which the SED are well fitted by a single modified blackbody at 95 and 85 K respectively (**?**, see)]CW95,Dent00. The errors in the observed fluxes are taken to be ∼30% and the errors on the mass are ∼45%

[b]Flux at 1.1 mm

References. — (1) Beckwith et al. 1990; (2) Guilloteau, Dutrey & Simon 1999; (3) Osterloh & Beckwith 1995; (4) Weintraub, Sandell & Duncan 1989; (5) Henning et al. 1994; (6) Natta et al. 1999; (7) Mannings & Sargent 1997; (8) Henning et al. 1998; (9) Natta et al. 1997; (10) Bockelée-Morvan et al. 1995; (11) Sylvester et al. 1996; (12) Chini et al. 1991

Table 8. Stellar ages

Name	Stellar age[a] (Myr)	Previous estimate (Myr)	Ref.
AA Tau	2.4	1.2	1
DM Tau	2.5		
DR Tau	3.8	2.5	1
GG Tau a	1.7	0.82	1
GO Tau	3.2		
RY Tau	7.8	6.5	1
GM Aur	1.8	1.3	
LkCa 15	11.7	8.3	1
TW Hya	9.3	15	2
UX Ori	4.6	2	3
HD 163296	6.0	5	4
CQ Tau	8.9	10	4
MWC 480	4.6	6	4
MWC 863	6.0	5	4
HD 36112	6.0	6	4
AB Aur	4.6	≃3–5	4
WW Vul	···	···	···
V892 Tau	···	···	···
49 Ceti	7.8	···	···
HD 135344	16.7	···	···
β Pictoris	20	≃20–100	5

[a]The stellar ages were derived using the evolutionary tracks of Siess, Forestini & Bertout 2000.

References. — (1) Siess, Forestini & Bertout 1999; (2) Webb et al. 1999; (3) Natta et al. 1999; (4) Mannings & Sargent 1997; (5) Barrado y Navascués et al. 1999

Table 9. Summary of disk gas masses deduced by various techniques

Name	$M_{1.3\mathrm{mm}}$(total) ($10^{-3}M_\odot$)	M_{CO}(total) ($10^{-3}M_\odot$)	$M_{\mathrm{H_2}}$(warm gas) ($10^{-3}M_\odot$)
AA Tau	17±8	···	0.2–20
DM Tau	21±9	0.18±0.05	···
DR Tau	31±14	0.07±0.02	···
GG Tau a	116±52	0.16±0.05	3.6±1.8
GO Tau	16±7	0.09±0.03	6.4±3.2
RY Tau	40±18	0.06±0.02	···
GM Aur	49±22	0.16±0.05	···
LkCa 15	33±15	0.14±0.04	8.6±4.3
UX Ori	42±19	···	9–117
HD 163296	65±29	0.56±0.16	0.4±0.2
CQ Tau	22±10	···	2.0±1.0
MWC 480	22±10	0.17±0.05	0.7–78.8
MWC 863	10±5	···	1.5±0.8
HD 36112	29±13	0.23±0.07	0.2–18.7
AB Aur	21±9	1.72±0.51	1.3±0.7
49 Ceti	0.4±0.2	10^{-3}	0.3–2.3
HD 135344	2.8±1.3	$2.1\pm0.6\times10^{-3}$	6.4±3.2
β Pictoris	0.03±0.015	···	0.17±0.08

Note. — See Tables 3, 5 and 7 for details. The details of the derivations are given in sections 5.4 (for $M_{1.3\mathrm{mm}}$), 5.3 (for M_{CO}) and 4.4 (for $M_{\mathrm{H_2}}$).

Fig. 1.— The H_2 S(0) 28 μm spectra observed with the ISO-SWS toward pre-main-sequence and debris-disk stars. The underlying continuum has been subtracted. The rest wavelength of the J =2–0 transition is indicated by the dashed line. Small wavelength shifts may be attributed to instrumental effects (see text). The dash-dotted gaussian corresponds to emission by a source filling the beam; the H_2 lines have to lie inside this gaussian to be considered detected.

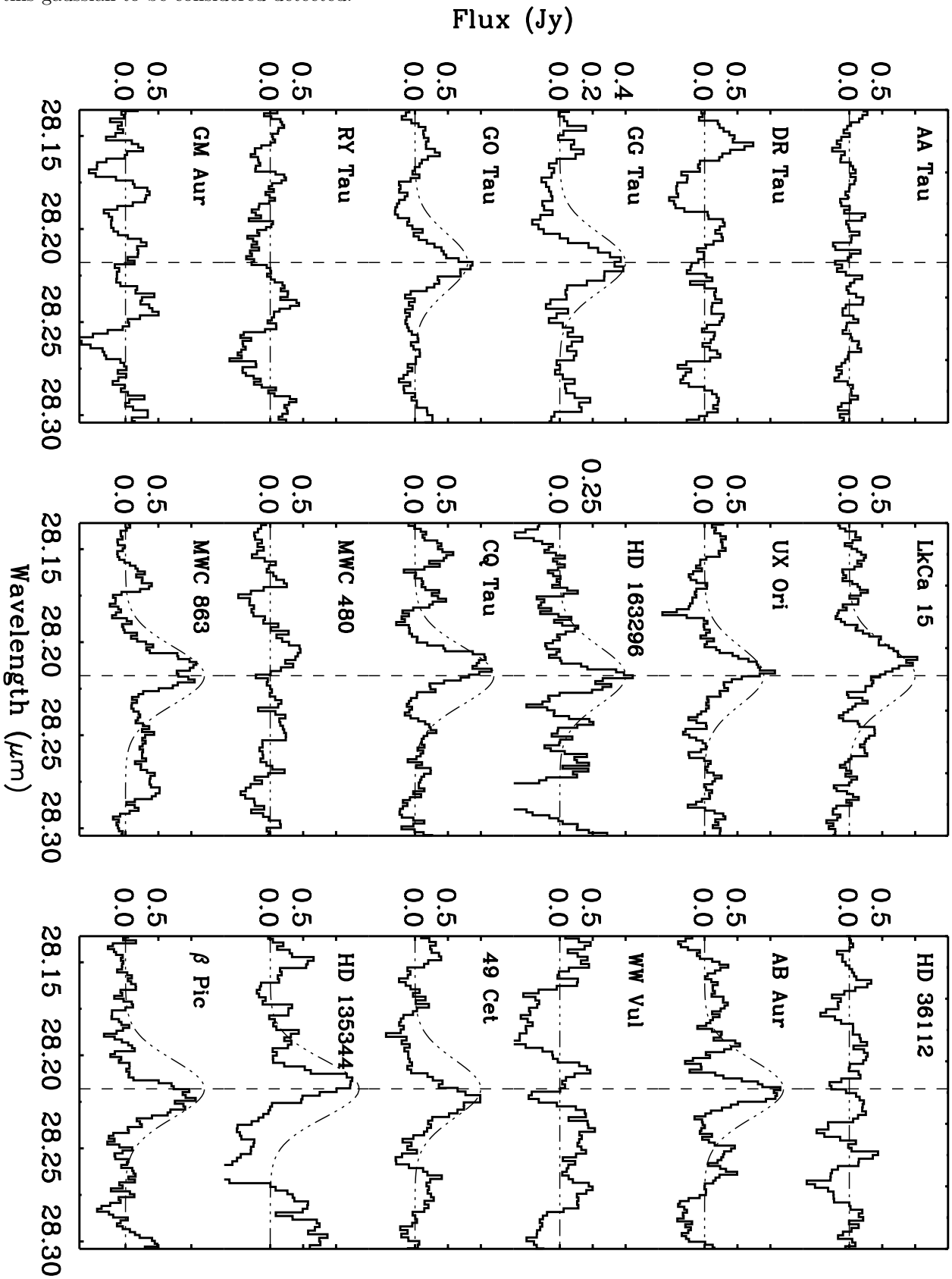

Fig. 2.— As Figure 1, but for the H_2 S(1) J=3–1 tranistion.

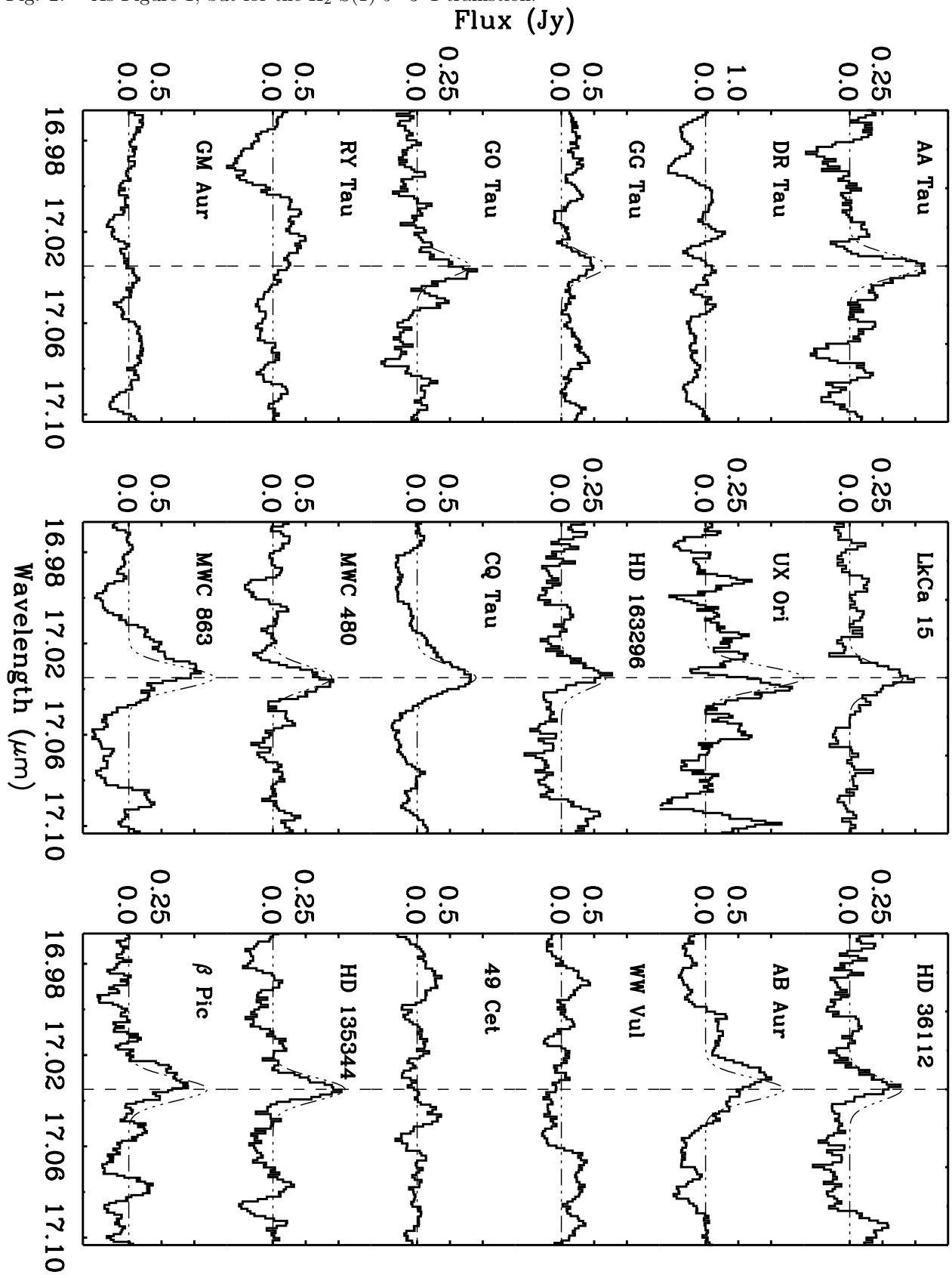

Fig. 3.— Mass of H_2 as a function of the excitation temperature for an observed H_2 S(1) integrated flux of 10^{-13} erg s^{-1} cm^{-2} for a source at 140 pc. The dash-dotted line corresponds to the typical Solar Nebula mass (10^{-2} $M_\odot$) and the dashed line indicates the mass of Jupiter.

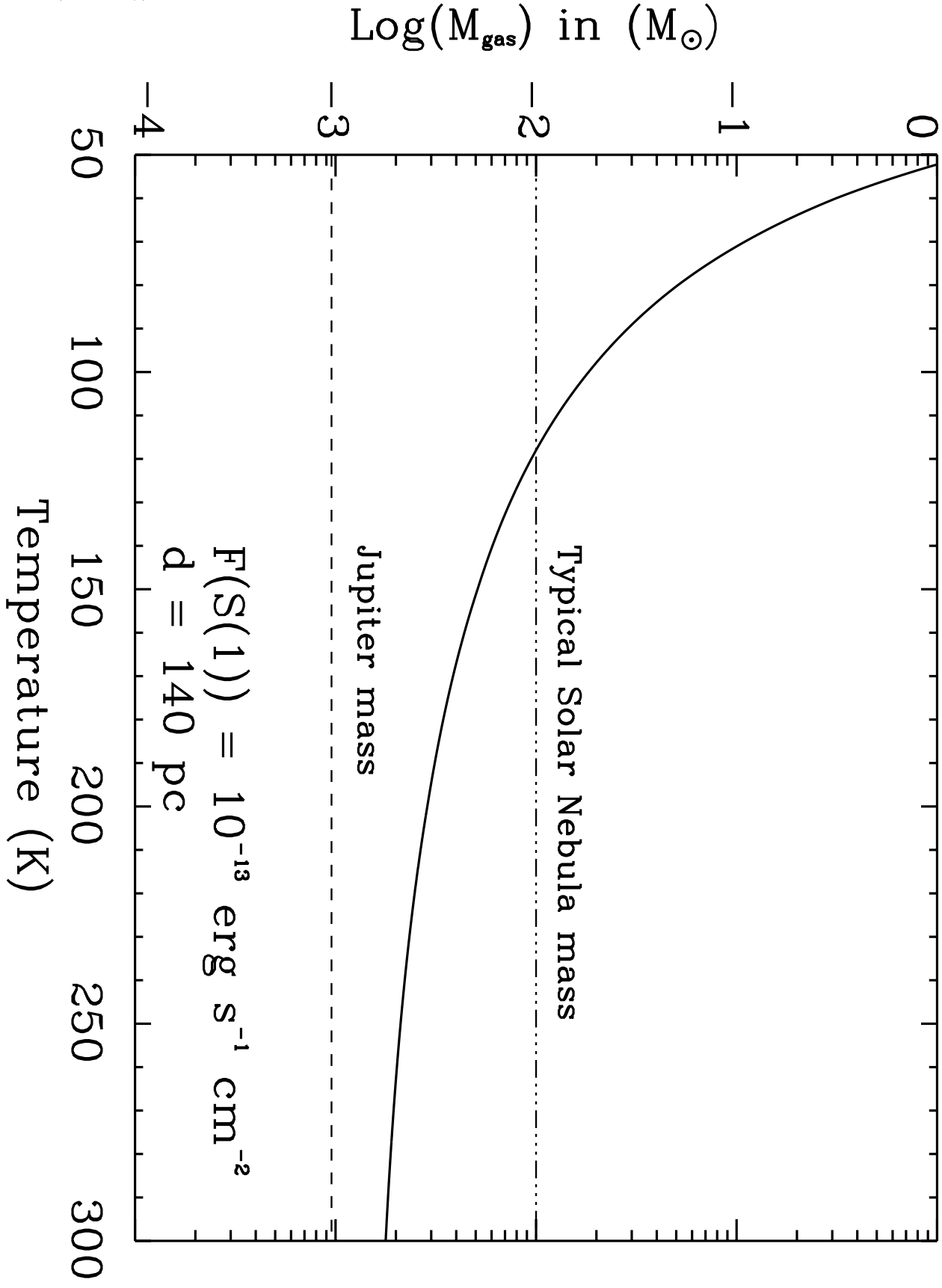

Fig. 4.— Dust temperature as a function of the ratio of the continuum fluxes at 17μm and at 28μm, assuming optically thin emission. The vertical bars at the bottom indicate the observed ratios for our sources. The errors on the ratio are typically 50%.

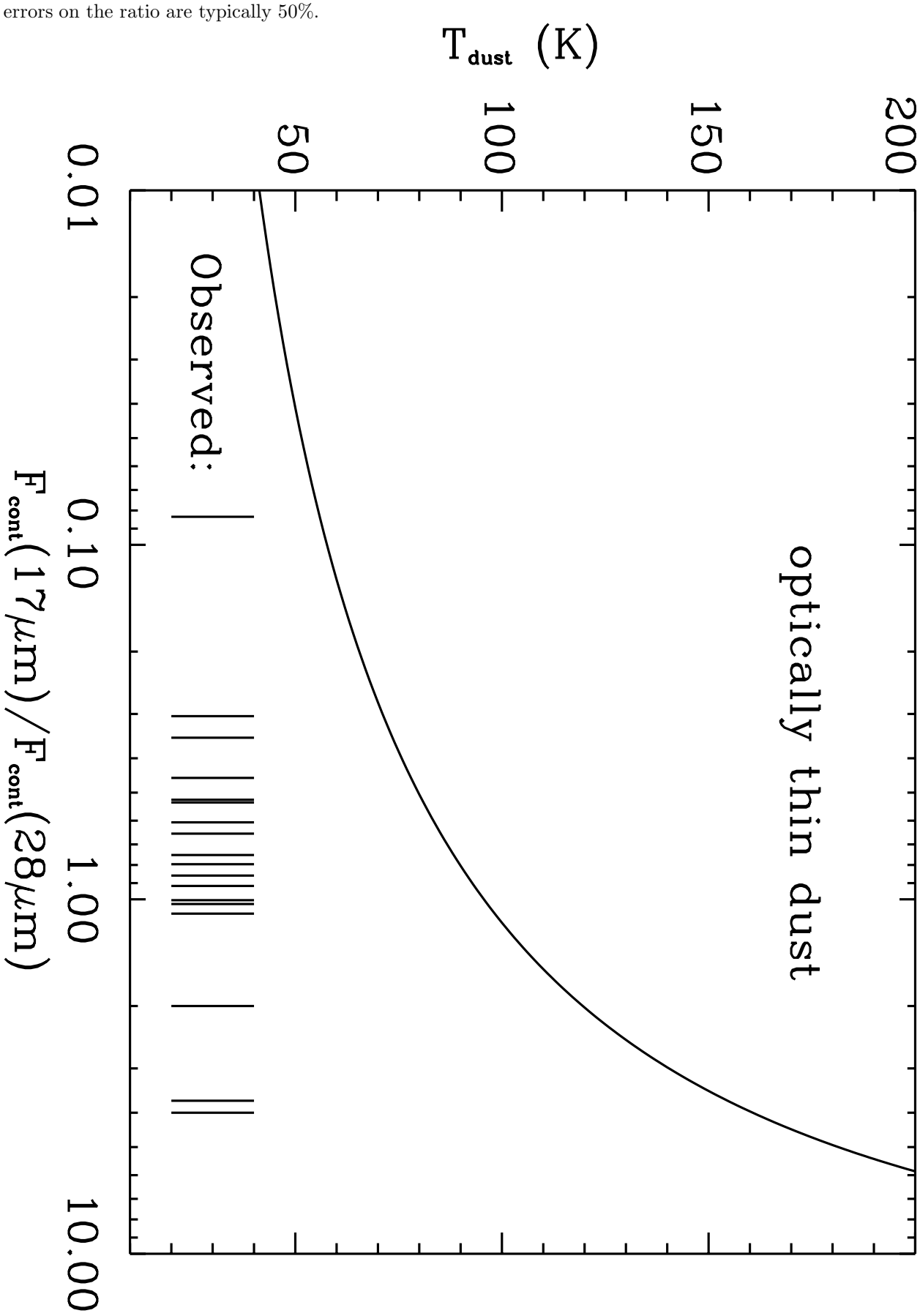

Fig. 5.— Warm gas temperatures versus warm dust temperature for sources having both S(0) and S(1) lines detected. The errors on the temperatures are ∼10%.

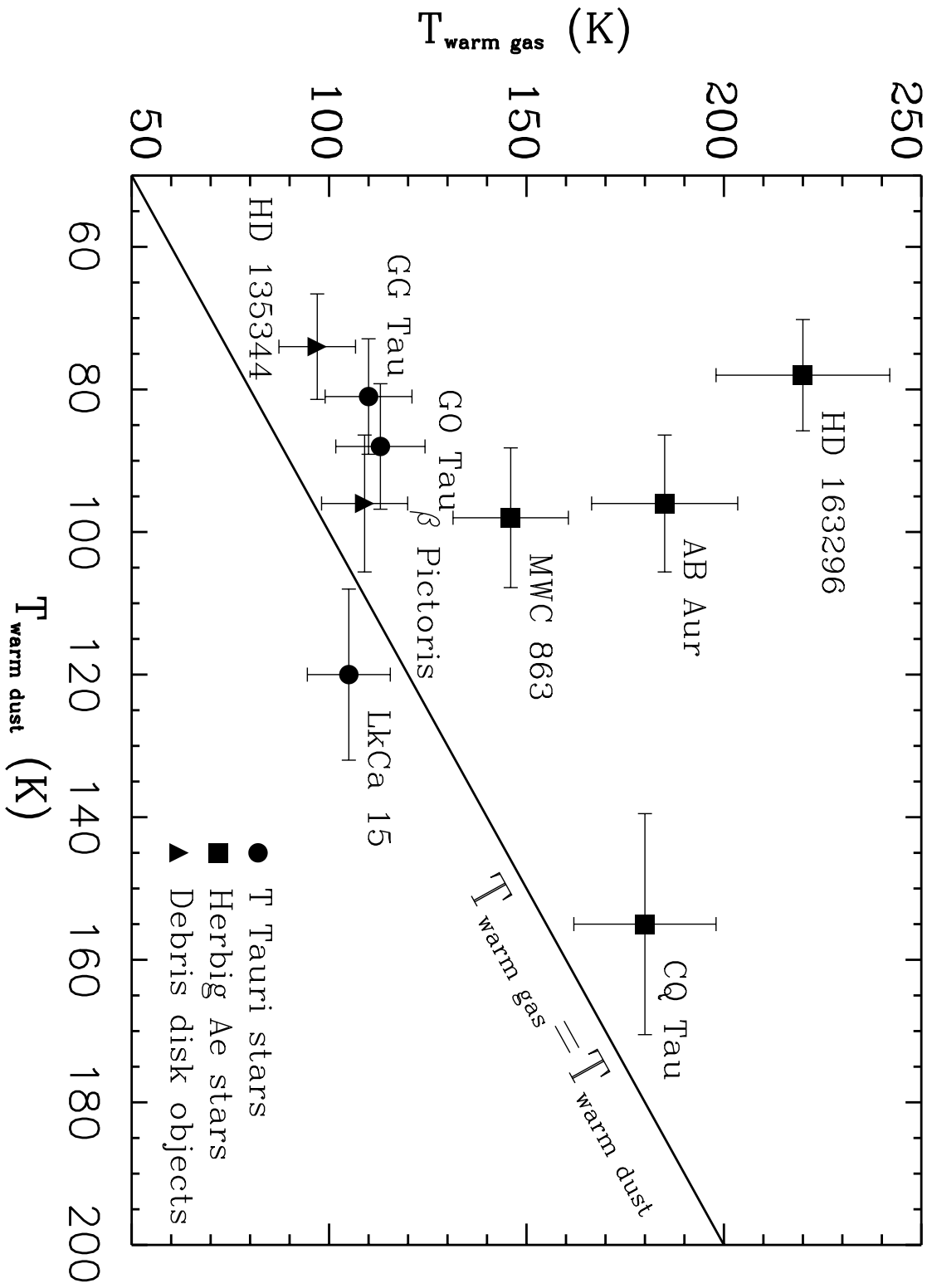

Fig. 6.— Single-dish JCMT spectra of the ^{12}CO 3–2 line at 345 GHz toward protoplanetary disks. The vertical scale is $T_{\rm MB}$ in K. The horizontal scale denotes the LSR velocity. The characteristic double-peaked line profile due to a rotating disk is seen for many sources.

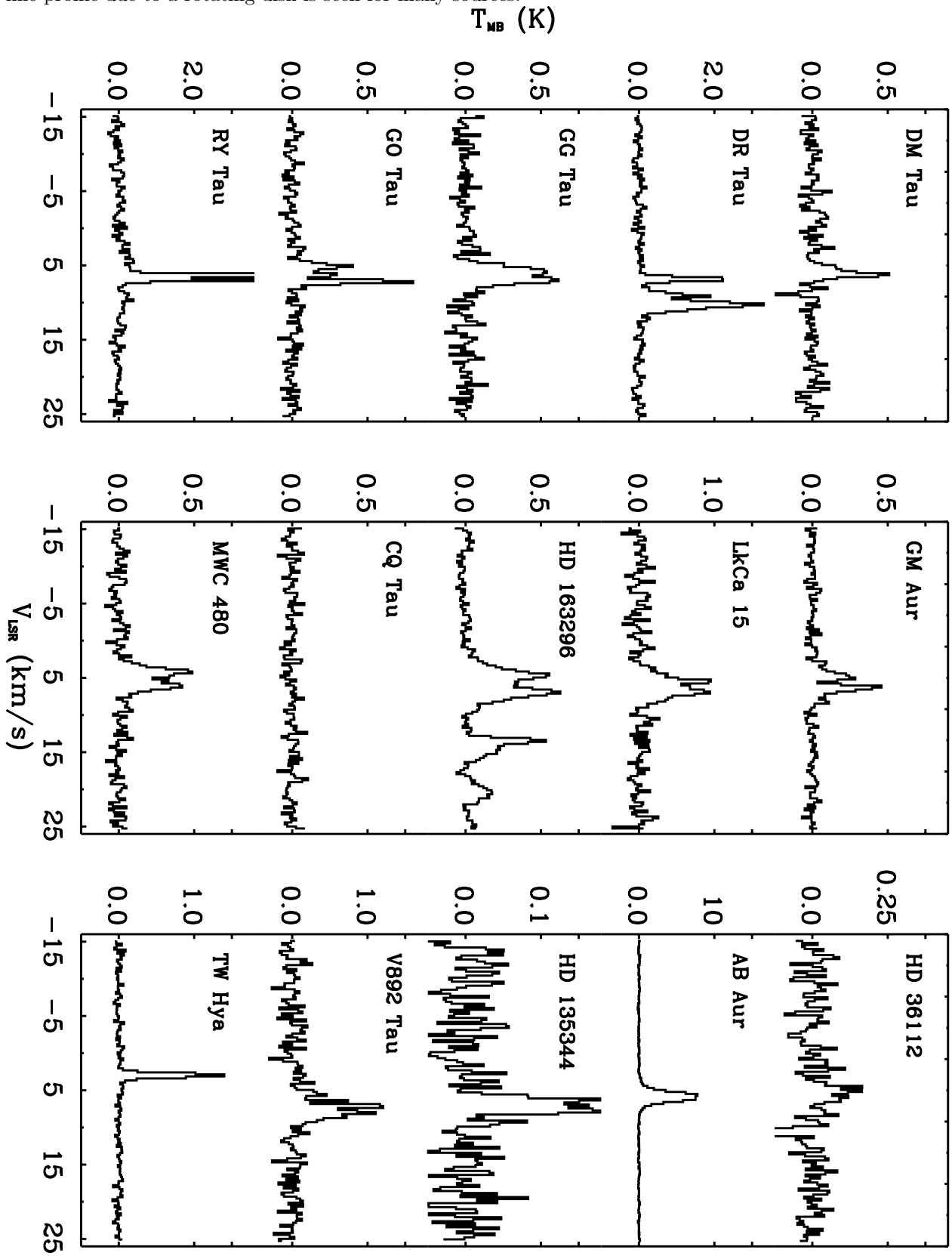

Fig. 7.— As Figure 6, but for ^{13}CO 3–2 JCMT spectra.

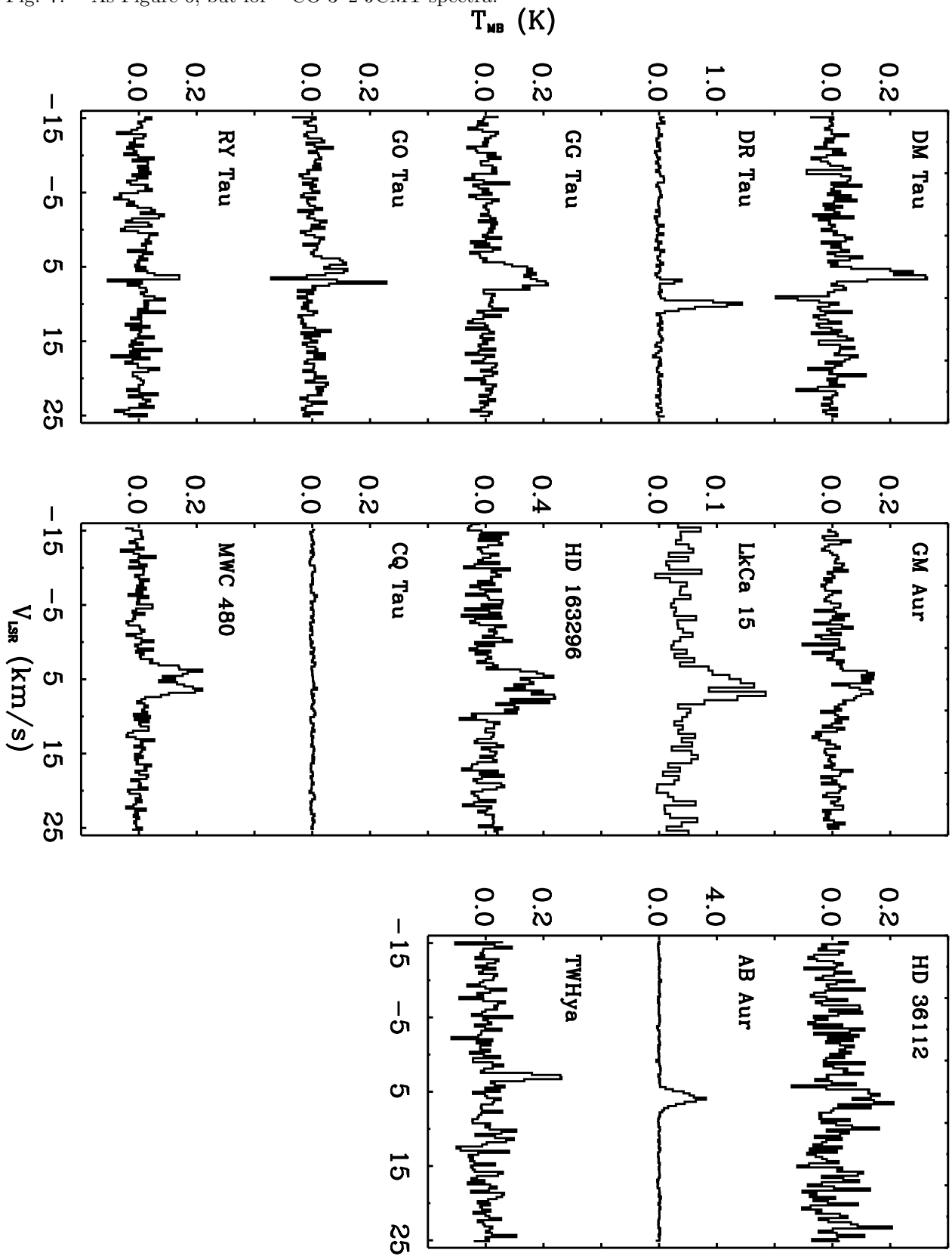

Fig. 8.— As Figure 6, but for CO 6–5 CSO spectra.

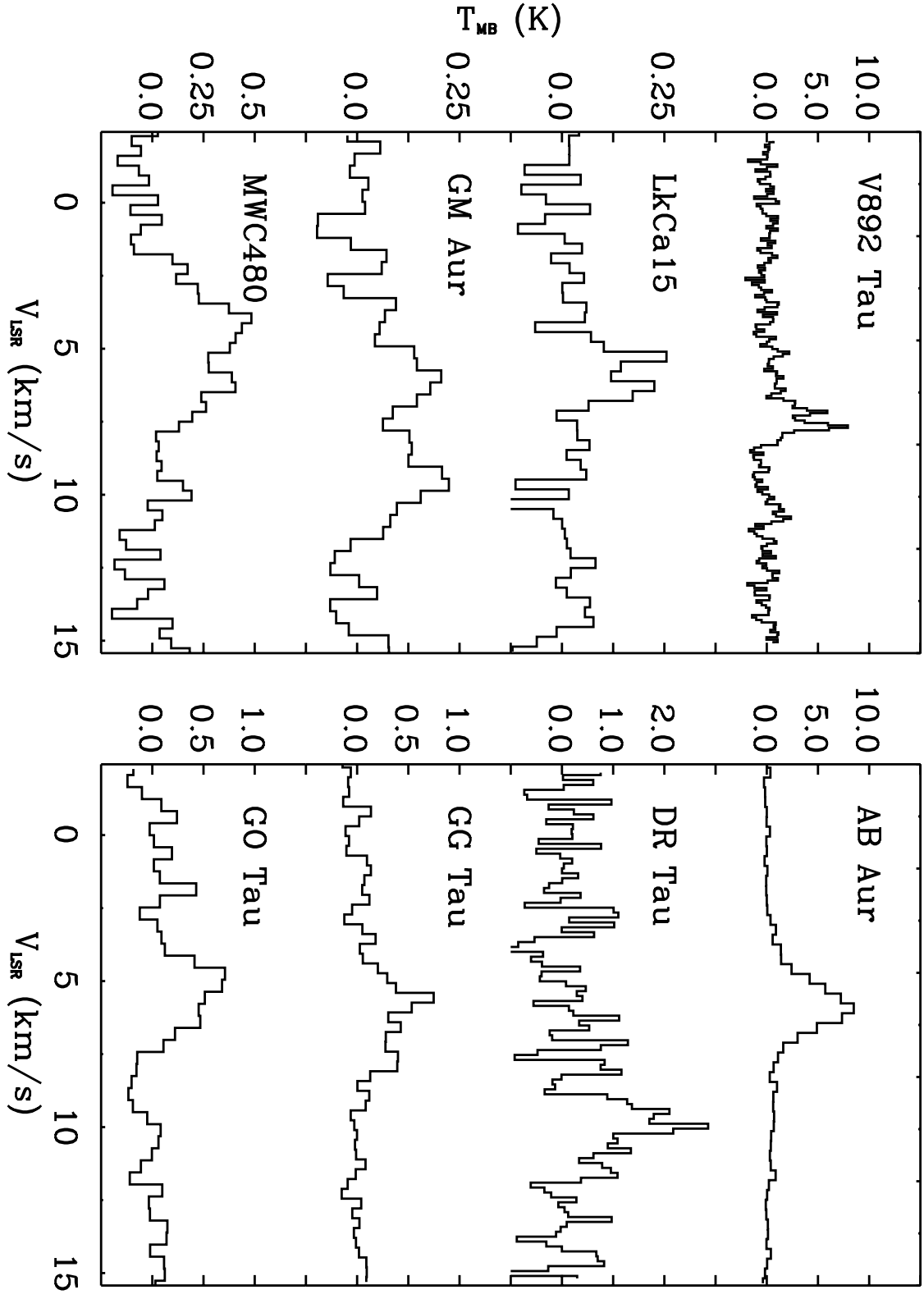

Fig. 9.— Velocity integrated ^{12}CO 3–2 flux in K km s^{-1} plotted against velocity integrated ^{13}CO 3–2 flux normalized at 100 pc.

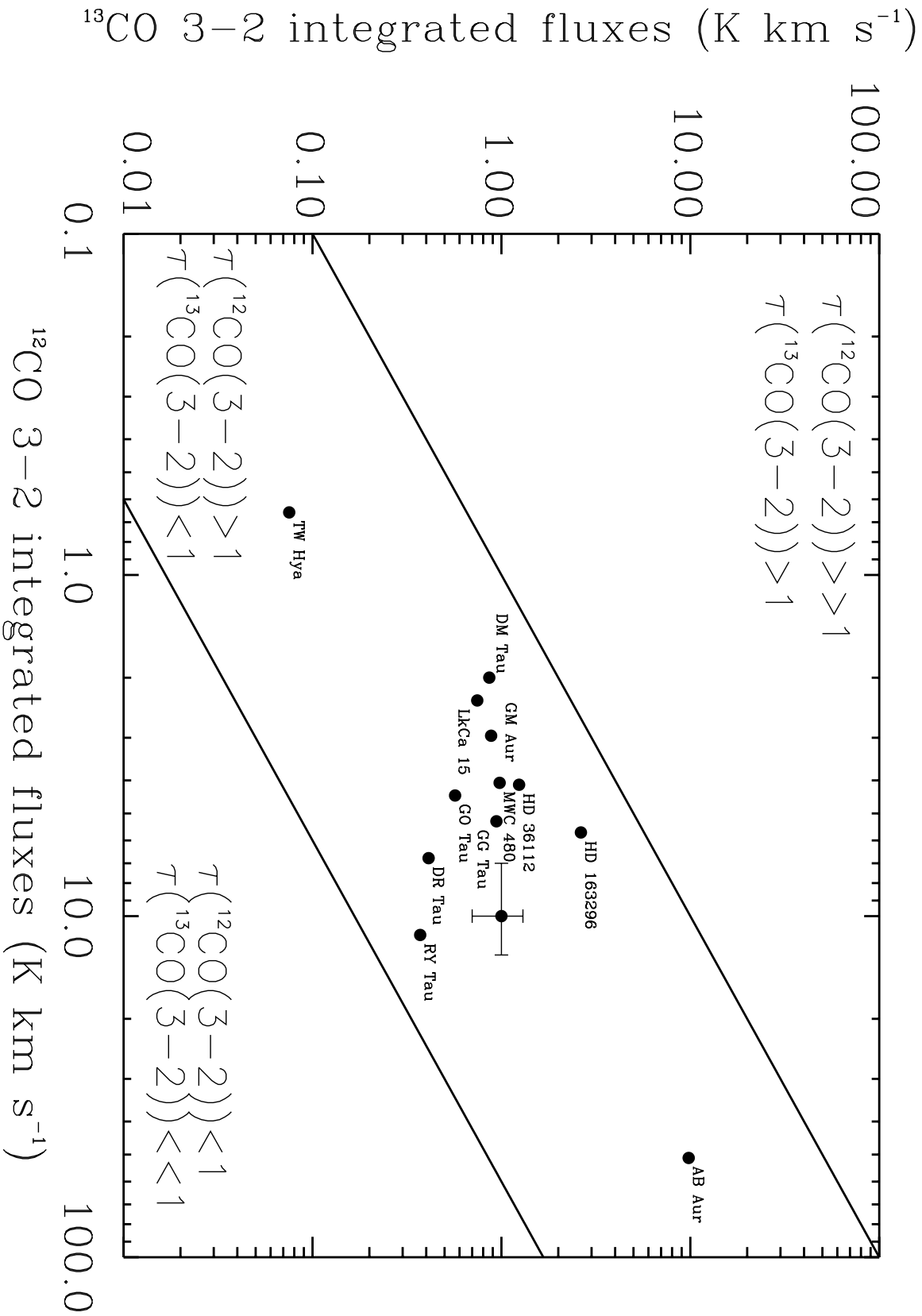

Fig. 10.— Estimated gas mass obtained from CO observations (upper panel) and H_2 observations (lower panel) plotted against the disk mass computed from 1.3mm dust assuming a gas/dust ratio of 100:1. In the upper panel, the dashed lines separate the regions of different CO depletion factors.

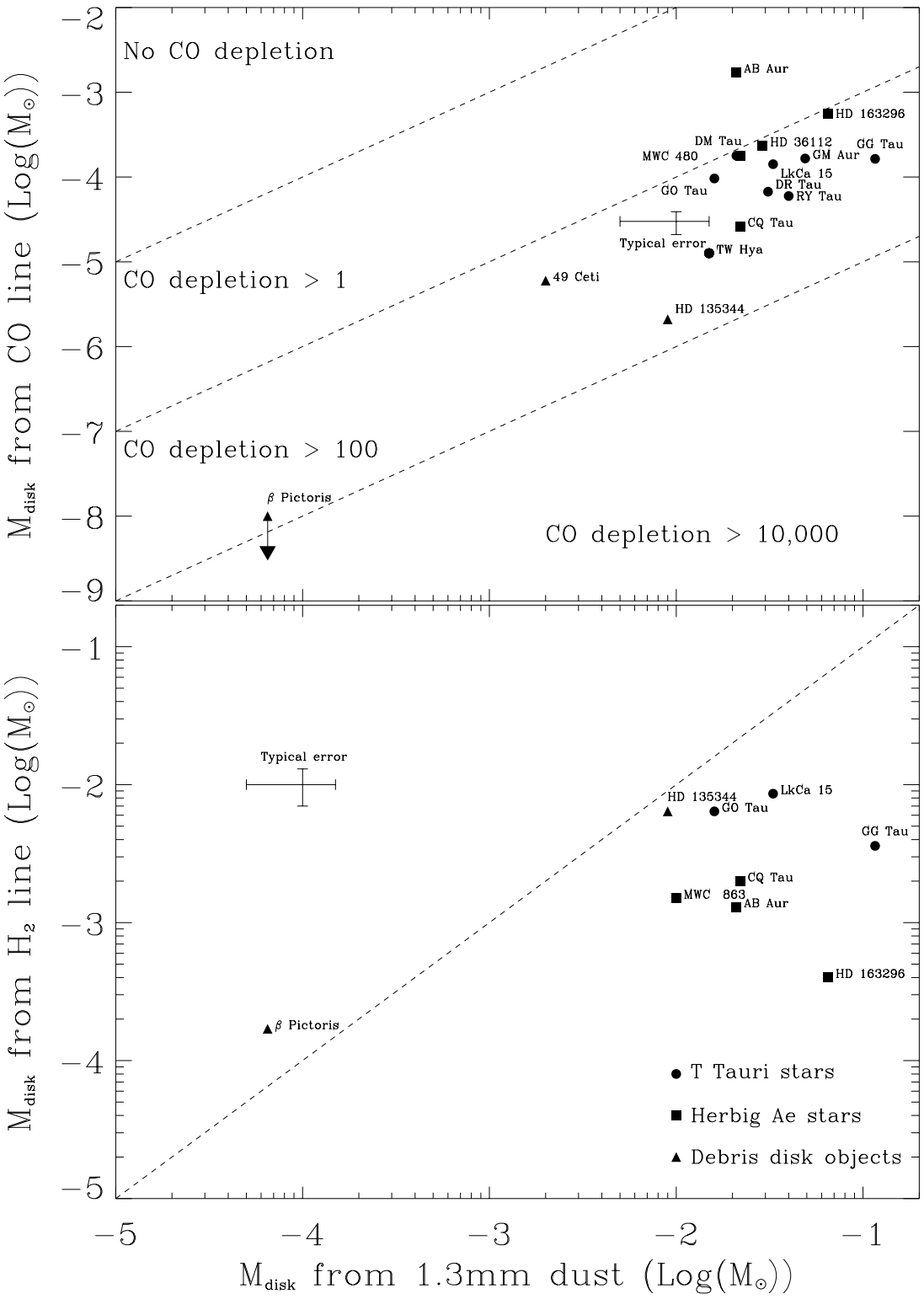

Fig. 11.— The evolutionary tracks of Siess, Forestini & Bertout (2000) for a metal abundance Z=0.02. The left panel corresponds to intermediate mass stars (2–3 $M_\odot$) and the right panel to low mass stars (1–2 $M_\odot$). The location of our sources are overplotted. The different tracks correspond to the masses indicated next to each track; the tickmarks along each track indicate the ages in Myrs.

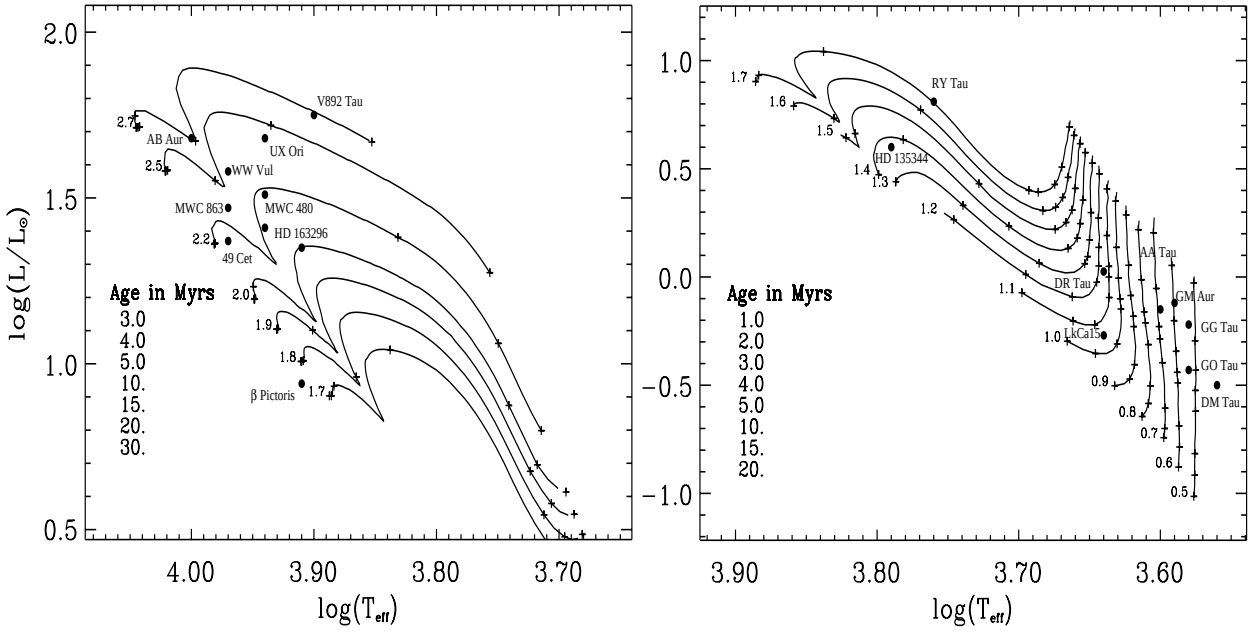

Fig. 12.— Variation of the total disk mass with the age of the central object deduced from the three methods.

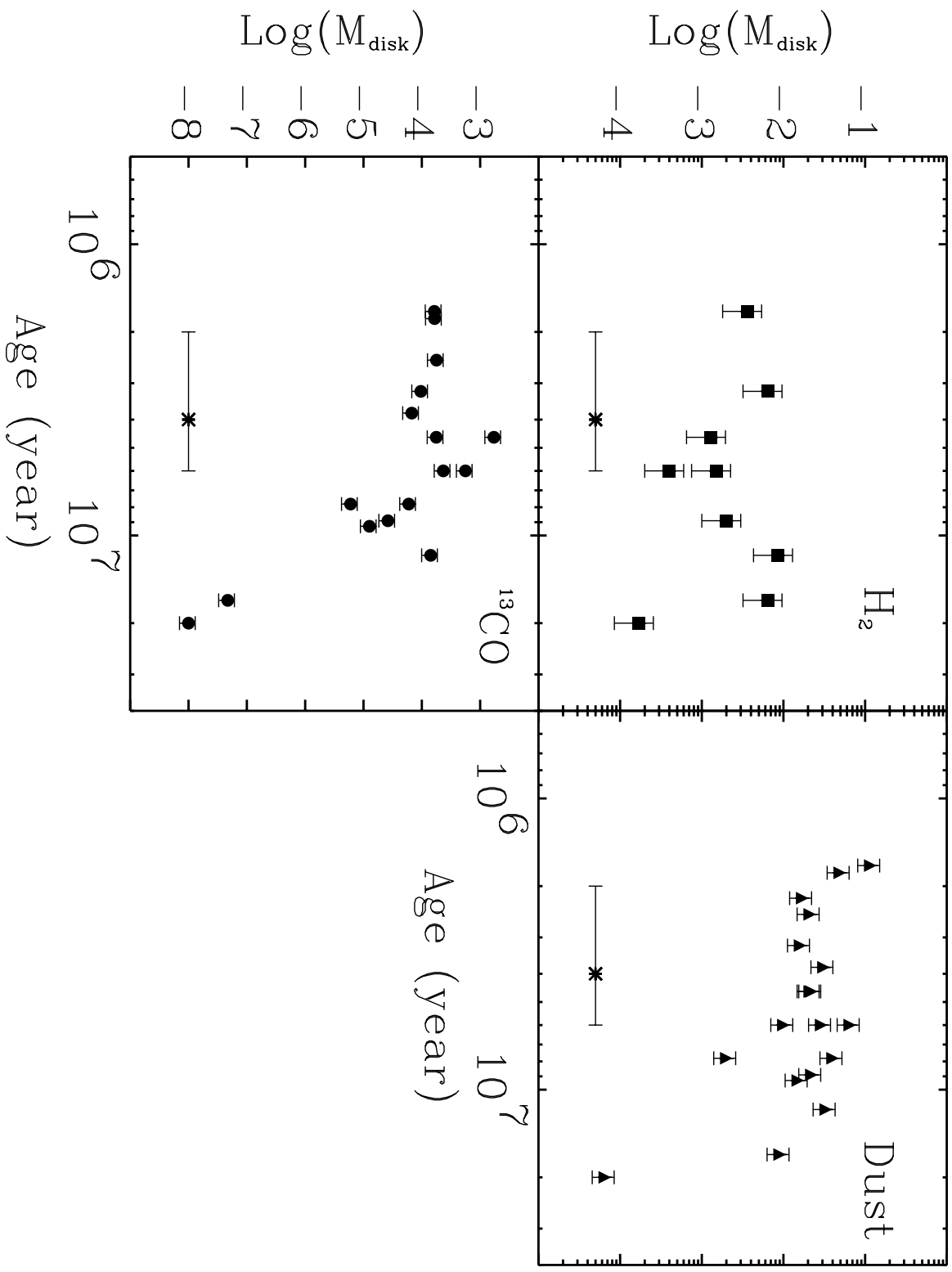

Fig. 13.— Evolution of the ratio of the total gas mass to the solid mass in circumstellar disks. The standard interstellar ratio is 100:1.

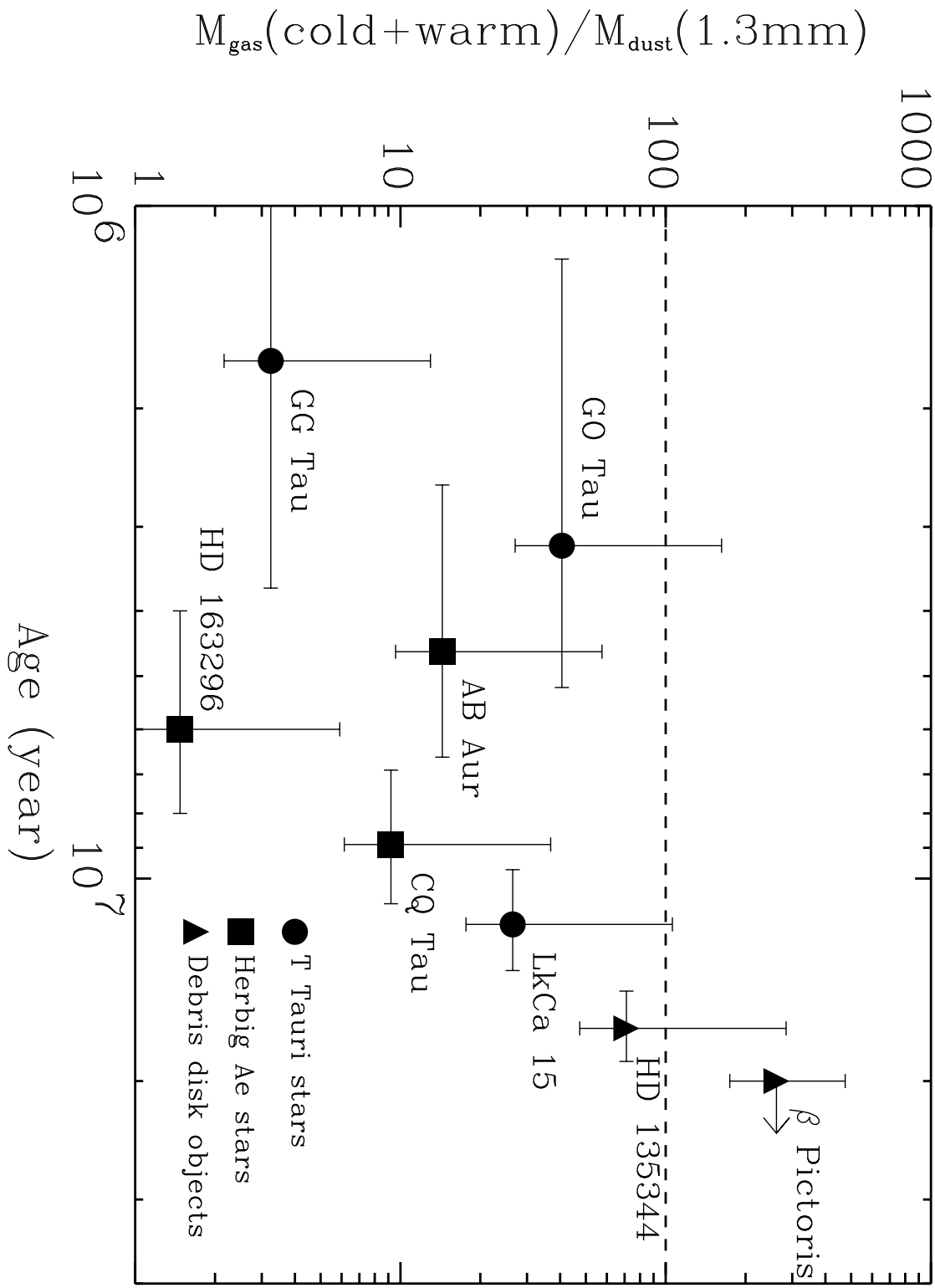

Fig. 14.— Panels (a) and (c) show the warm gas mass derived from H_2 and the corresponding H_2 excitation temperature as a function of the effective temperature of the central star. Panels (b) and (d) plot the variation of the warm gas mass and excitation temperature against the continuum flux at 28 μm normalized at 100 pc.